A public code for general relativistic, polarised radiative transfer around spinning black holes

Jason Dexter[*]

Max Planck Institute for Extraterrestrial Physics, Giessenbachstr. 1, D-85748 Garching, Germany

ABSTRACT

Ray tracing radiative transfer is a powerful method for comparing theoretical models of black hole accretion flows and jets with observations. We present a public code, GRTRANS, for carrying out such calculations in the Kerr metric, including the full treatment of polarised radiative transfer and parallel transport along geodesics. The code is written in FORTRAN 90 and efficiently parallelises with OPENMP, and the full code and several components have PYTHON interfaces. We describe several tests which are used for verifying the code, and we compare the results for polarised thin accretion disc and semi-analytic jet problems with those from the literature as examples of its use. Along the way, we provide accurate fitting functions for polarised synchrotron emission and transfer coefficients from thermal and power-law distribution functions, and compare results from numerical integration and quadrature solutions of the polarised radiative transfer equations. We also show that all transfer coefficients can play an important role in predicted images and polarisation maps of the Galactic centre black hole, Sgr A*, at submillimetre wavelengths.

Key words: accretion, accretion discs – black hole physics – radiative transfer – relativistic processes – Galaxy: centre – galaxies: jets.

1 INTRODUCTION

Quantitative comparisons of theoretical models of black hole accretion flows and jets with observations require radiative transfer calculations. The bulk of the radiation is often produced near the black hole event horizon, where relativistic effects of Doppler beaming, gravitational redshift, and light bending become important. Ray tracing is a convenient method for carrying out fully relativistic radiative transfer calculations. Light bending is naturally accounted for by taking the rays to be null geodesics in the Kerr metric, and the radiative transfer equation can then be solved along geodesics to calculate observed intensities.

This technique has been used to calculate images (e.g. Luminet 1979) and spectra (e.g. Cunningham 1975) of thin black hole accretion discs (Shakura & Sunyaev 1973; Page & Thorne 1974), including state-of-the-art methods to fit spectra in order to infer parameters such as the black hole spin (Li et al. 2005; Davis & Hubeny 2006; Dauser et al. 2010). Ray tracing is also convenient for including general relativistic rotations of the polarisation direction via parallel transport (Connors & Stark 1977; Connors, Stark & Piran 1980), and has been applied to the polarised radiative transfer of synchrotron radiation from thick accretion discs, e.g. in order to model the Galactic Centre black hole Sgr A* (Broderick & Loeb 2005, 2006). With the development of general relativistic MHD

simulations of black hole accretion (De Villiers & Hawley 2003; Gammie, McKinney & Tóth 2003), ray tracing has become popular as a post-processing step to study their variability properties (Schnittman, Krolik & Hawley 2006; Noble & Krolik 2009; Dexter & Fragile 2011) and radiative efficiency (Kulkarni et al. 2011; Noble et al. 2011), as well as for comparison with observations of Sgr A* (e.g. Noble et al. 2007; Mościbrodzka et al. 2009; Dexter, Agol & Fragile 2009; Chan et al. 2015; Gold et al. 2016) and M87 (e.g. Dexter, McKinney & Agol 2012b; Moscibrodzka, Falcke & Shiokawa 2015).

Of particular interest are radiative transfer calculations relevant for current and future event horizon scale interferometric observations of Sgr A* and M87 at submillimeter (*The Event Horizon Telescope*; Doeleman et al. 2009) and near-infrared (the VLTI GRAVITY instrument; Eisenhauer et al. 2008) wavelengths. Fully modelling the observed synchrotron radiation requires polarised radiative transfer. Existing codes for this application are either private (Broderick & Blandford 2004) or written as post-processors to specific numerical simulations (Shcherbakov, Penna & McKinney 2012). Other public tools (e.g. GYOTO and KERTAP; Vincent et al. 2011; Chen et al. 2015) do not include fully polarised radiative transfer.

We present a publicly available, fully general relativistic code, GRTRANS,[1] for polarised radiative transfer via ray tracing in the Kerr

---

* E-mail: jdexter@mpe.mpg.de

metric. We describe the methods used for the parallel transport of the polarisation basis into the local frame of the fluid (Section 2.2) and the integration of the polarised radiative transfer equations (Section 2.5) using emission, absorption, and rotation coefficients (Section 2.3) calculated based on radiative processes in terms of a background fluid model (Section 2.4). In Section 3, we discuss tests used to validate the code, and comparisons of full example problems to those in the literature. We also provide fitting functions for polarised synchrotron emission, absorption, and transfer coefficients (Appendix A and B), and show an example polarised image from a model of the submm emission of Sgr A*, to demonstrate how all of the transfer coefficients play important roles in the final polarised image. Finally, Section 4 gives a summary of the code convergence and performance properties, and an overview of its organization.

2 METHODS

The goal of a ray tracing radiative transfer code is to calculate the observed intensity on locations (pixels) of an observer's camera for a given model of emission and absorption. We calculate the Boyer–Lindquist coordinates of the photon trajectories from the observer towards the black hole (trace the rays) corresponding to each pixel, parallel transport the observed polarisation basis into the fluid frame, calculate the local emission and absorption properties at each location, and then solve the radiative transfer equations for the given emission and absorption along those rays.

2.1 Ray tracing

The observer's camera at inclination $\mu_0 = \cos\theta_0$ and orientation ϕ_0 has pixels whose coordinates are described by apparent impact parameters α, β parallel and perpendicular to the black hole spin axis. The photon trajectories in GRTRANS are assumed to be geodesics in the Kerr metric, in which case their constants of motion are specified for given α, β (Bardeen, Press & Teukolsky 1972):

$$l = -\alpha\sqrt{1-\mu_0^2}, \tag{1}$$

$$q^2 = \beta^2 + \mu_0^2(\alpha^2 - a^2), \tag{2}$$

where l, q^2, and a are the dimensionless z-component of the angular momentum, Carter's constant, and black hole spin parameters.

The trajectories for each ray given the constants can then be found by solving the geodesic equation. We do this semi-analytically by reducing the equations of motion to Jacobian integrals and Jacobi-elliptic functions (Rauch & Blandford 1994; Agol 1997) as implemented in the code GEOKERR (Dexter & Agol 2009).

In this method, the independent variable is either the inverse radius $u = 1/r$ or $\mu = \cos\theta$. The former is used by default, since even steps in u naturally concentrate resolution towards the black hole, where most of the radiation is produced. In special cases, for example a thin accretion disc in the equatorial plane, the latter method is preferable since then one can solve for the radius where $\mu = 0$, without needing to integrate the geodesic. In the default case with u as the independent variable, the sampling can become poor near radial turning points (e.g. sections of the orbit at nearly constant radius). For this reason, near radial turning points μ is instead used as the independent variable to fill in the geodesic.

The calculation is started at a small, non-zero value of u in order to keep the coordinate time and affine parameter finite. The geodesics are tabulated starting at a value of u of interest for the problem (e.g. the outer radial boundary of a numerical simulation)

and are terminated either just outside the event horizon for bound orbits, or once they again reach the outer radius of interest for the calculation. The locations to sample (u_i) and number of samples (n) are code parameters. The assumption made by the code is that the initial intensity is zero at the farthest point sampled along the ray. When using quadrature methods for integrating the radiative transfer equation, this n sets the total number of steps used. When using the numerical method, that algorithm calculates the intensity at these n points but can use many intermediate steps as well. See Section 2.5 for more details.

For most problems of interest here, many points along each ray are needed for accurate radiative transfer, and using semi-analytic geodesics is unlikely to save a significant amount of computational time (e.g. Dolence et al. 2009; Chan et al. 2015). The semi-analytic method is more accurate, but geodesic error is typically small compared to that in emission or absorption coefficients or the radiative transfer integration (see below). We implement semi-analytic geodesics in GRTRANS due to our past work on the GEOKERR code (Dexter & Agol 2009), but it would be straightforward to add a numerical integration method to GRTRANS.

2.2 Parallel transport of the polarisation basis

The observed polarisation is measured with respect to the horizontal and vertical axes defining the camera, while the polarised emission and transfer coefficients are most naturally given relative to a local direction in the emitting fluid (e.g. the magnetic field direction for synchrotron radiation). To relate the two, we first parallel transport the observed polarisation basis along the geodesic, and then transform it to the orthonormal frame comoving with the fluid. The angle between the two bases can then be used to rotate the local coefficients into the observed polarisation basis.

Parallel transport of a vector describing the polarisation basis f^μ perpendicular to the wave vector k^μ is simplified in the Kerr metric by the existence of a complex constant called the Walker–Penrose constant (Walker & Penrose 1970), given in Boyer–Lindquist coordinates with $G = c = M = 1$ as (Connors & Stark 1977; Connors et al. 1980; Chandrasekhar 1983):

$$K_1 - iK_2 = (r - ia\cos\theta)\left\{(k^t f^r - k^r f^t) + a\sin^2\theta(k^r f^\phi - k^\phi f^r) \right.$$
$$\left. - i[(r^2 + f^2)(k^\phi f^\theta - f^\phi k^\theta) - a(k^t f^\theta - k^\theta f^t)]\sin\theta\right\}, \tag{3}$$

where

$$k^t = \frac{1}{\rho^2}\left[-a\left(a\sin^2\theta - l\right) + \frac{(r^2+a^2)}{\Delta}\left(r^2 + a^2 - al\right)\right], \tag{4}$$

$$k^r = -\frac{s_r}{\rho^2}R(r), \tag{5}$$

$$k^\theta = -\frac{s_\theta}{\rho^2}\sqrt{\frac{M(\theta)}{\sin^2\theta}}, \tag{6}$$

$$k^\phi = \frac{1}{\rho^2}\left[-a + \frac{l}{\sin^2\theta} + \frac{a}{\Delta}(r^2 + a^2 - al)\right], \tag{7}$$

$$M(\theta) = q^2 + (a^2 - q^2 - l^2)\cos^2\theta - a^2\cos^4\theta, \tag{8}$$

$$R(r) = r^2 + (a^2 - q^2 - l^2) + 2\left[(a-l)^2 + q^2\right]r^{-1} \tag{9}$$

$$- a^2 q^2 r^{-2}, \tag{10}$$

$$\rho^2 = r^2 + a^2 \cos^2 \theta, \tag{11}$$

$$\Delta = r^2 - 2r + a^2, \tag{12}$$

is the photon wave vector whose direction is specified by the signs s_r and s_θ (e.g. Rauch & Blandford 1994).

The real and imaginary parts of the constant, K_1 and K_2, provide two constraints on the transported basis vectors, while the orthogonality condition $\boldsymbol{k}^\mu f_\mu = 0$ provides a third. Since the polarisation basis vectors are already only defined up to a multiple of the wave vector, we can set $f^t = 0$ without any loss of generality, which leaves three linear equations for the three remaining components of f^μ:

$$K_1 = \delta_1 f^r + \delta_2 f^\theta + \delta_3 f^\phi, \tag{13}$$

$$K_2 = \gamma_1 f^r + \gamma_2 f^\theta + \gamma_3 f^\phi, \tag{14}$$

$$\boldsymbol{k}^\mu a_\mu = 0, \tag{15}$$

with

$$\delta_1 = r\boldsymbol{k}^t - ra \sin^2 \theta \boldsymbol{k}^\phi, \tag{16}$$

$$\delta_2 = a^2 \sin \theta \cos \theta \boldsymbol{k}^t - a \cos \theta \sin \theta (r^2 + a^2) \boldsymbol{k}^\phi, \tag{17}$$

$$\delta_3 = ra \sin^2 \theta \boldsymbol{k}^r + a \cos \theta \sin \theta (r^2 + a^2) \boldsymbol{k}^\theta, \tag{18}$$

$$\gamma_1 = a \cos \theta \boldsymbol{k}^t - a^2 \cos \theta \sin^2 \theta \boldsymbol{k}^\phi, \tag{19}$$

$$\gamma_2 = r(r^2 + a^2) \sin \theta \boldsymbol{k}^\phi - ar \sin \theta \boldsymbol{k}^t, \tag{20}$$

$$\gamma_3 = a^2 \cos \theta \sin^2 \theta \boldsymbol{k}^r - r(r^2 + a^2) \sin \theta \boldsymbol{k}^\theta. \tag{21}$$

The components of f^μ can then be calculated as:

$$f^r = \frac{1}{N} \left[(\gamma_2 K_1 - \delta_2 K_2)(g_{\phi\phi} \boldsymbol{k}^\phi + g_{\phi t} \boldsymbol{k}^t) \right. \tag{22}$$

$$\left. - (\gamma_3 K_1 - \delta_3 K_2) g_{\theta\theta} \boldsymbol{k}^\theta \right], \tag{23}$$

$$f^\theta = -\frac{1}{N} \left[(\gamma_1 K_1 - \delta_1 K_2)(g_{\phi\phi} \boldsymbol{k}^\phi + g_{\phi t} \boldsymbol{k}^t) \right. \tag{24}$$

$$\left. - (\gamma_3 K_1 - \delta_3 K_2) g_{rr} \boldsymbol{k}^r \right], \tag{25}$$

$$f^\phi = \frac{1}{N} \left[(\gamma_1 K_1 - \delta_1 K_2) g_{\theta\theta} \boldsymbol{k}^\theta \right. \tag{26}$$

$$\left. - (\gamma_2 K_1 - \delta_2 K_2) g_{rr} \boldsymbol{k}^r \right], \tag{27}$$

$$N = (\gamma_2 \delta_1 - \gamma_1 \delta_2) g_{\phi\phi} \boldsymbol{k}^\phi - (\gamma_3 \delta_1 - \gamma_1 \delta_3) g_{\theta\theta} \boldsymbol{k}^\theta$$
$$+ (\gamma_2 \delta_1 - \gamma_1 \delta_2) g_{\phi t} \boldsymbol{k}^t + (\gamma_3 \delta_2 - \gamma_2 \delta_2) g_{rr} \boldsymbol{k}^r, \tag{28}$$

where $g_{\mu\nu}$ are the covariant metric components:

$$g_{tt} = -\frac{1}{\rho^2} \left(\Delta - a^2 \sin^2 \theta \right), \tag{29}$$

$$g_{\phi t} = \frac{-2ar \sin^2 \theta}{\rho^2}, \tag{30}$$

$$g_{rr} = \frac{\rho^2}{\Delta}, \tag{31}$$

$$g_{\theta\theta} = \rho^2, \tag{32}$$

$$g_{\phi\phi} = \frac{\Sigma \sin^2 \theta}{\rho^2}, \tag{33}$$

$$\Sigma = (r^2 + a^2)^2 - a^2 \Delta \sin^2 \theta. \tag{34}$$

The polarisation basis at the camera is defined so that positive Stokes Q is measured relative to the $\hat{\boldsymbol{\phi}}_0$ axis. Transforming the linear polarisation basis vectors $\hat{\boldsymbol{\phi}}_0$ and $\hat{\boldsymbol{\theta}}_0$ at the camera then requires knowledge of K_1 and K_2 for these vectors. These can be found from the asymptotic form of equation (3) (Chandrasekhar 1983). They are given by $K_1 = -\gamma$, $K_2 = -\beta$ and $K_1 = -\beta$, $K_2 = \gamma$, respectively, where $\gamma = -\alpha - a \sin \theta_0$ (Connors et al. 1980). Then equations (22)–(28) allow us to calculate the polarisation basis vectors at any point along the ray.

2.2.1 Transformation to the orthonormal fluid frame

The emission coefficients and the transfer matrix computed in the fluid frame are defined in a basis aligned with a local reference vector. For the case of synchrotron emission, it is convenient to use the local magnetic field direction and so we use b^μ as this vector in GRTRANS without loss of generality. In the case of electron scattering in a thin accretion disc, the polarisation is given relative to the disc normal vector, and so we assign the variable b^μ to that vector.

Before integrating the radiative transfer equations, these coefficients must be transformed to the observed polarisation basis. This transformation requires finding the angle between the transported polarisation basis vectors and the polarisation reference vector (Shcherbakov & Huang 2011). We transform into the orthonormal frame comoving with the fluid where the four-velocity is $u^{(\alpha)} = (1, 0, 0, 0)$. The basis four-vectors of the transformation are (Krolik, Hawley & Hirose 2005; Beckwith, Hawley & Krolik 2008; Shcherbakov & Huang 2011; Kulkarni et al. 2011):

$$\boldsymbol{e}^\mu_{(t)} = u^\mu, \tag{35}$$

$$\boldsymbol{e}^\mu_{(r)} = (u_r u^t, -(u_t u^t + u_\phi u^\phi), 0, u_r u^\phi)/N_r, \tag{36}$$

$$\boldsymbol{e}^\mu_{(\theta)} = (u_\theta u^t, u_\theta u^r, 1 + u_\theta u^\theta, u_\theta u^\phi)/N_\theta, \tag{37}$$

$$\boldsymbol{e}^\mu_{(\phi)} = (u_\phi, 0, 0, -u_t)/N_\phi, \tag{38}$$

where the upper (lower) indices are lowered (raised) with the Kerr (Minkowski) metric and,

$$N_r^2 = -g_{rr}(u_t u^t + u_\phi u^\phi)(1 + u_\theta u^\theta), \tag{39}$$

$$N_\theta^2 = g_{\theta\theta}(1 + u_\theta u^\theta), \tag{40}$$

$$N_\phi^2 = -(u_t u^t + u_\phi u^\phi)\Delta \sin^2 \theta, \tag{41}$$

$$\Delta = r^2 - 2r + a^2. \tag{42}$$

Four-vectors in the coordinate frame are transformed to the comoving orthonormal frame by,

$$A^{(\beta)} = \eta^{(\alpha)(\beta)} g_{\mu\nu} \boldsymbol{e}^\mu_{(\alpha)} A^\nu. \tag{43}$$

where $\eta^{(\alpha)(\beta)}$ is the Minkowski metric.

The angle χ between the projected magnetic field and the polarisation basis is given in terms of ordinary dot products of the

magnetic field and parallel-transported basis three-vectors (denoted by hats):

$$\sin 2\chi = -2 \frac{\left(\hat{\boldsymbol{a}} \cdot \hat{\boldsymbol{B}}\right)\left(\hat{\boldsymbol{b}} \cdot \hat{\boldsymbol{B}}\right)}{\left(\hat{\boldsymbol{a}} \cdot \hat{\boldsymbol{B}}\right)^2 + \left(\hat{\boldsymbol{b}} \cdot \hat{\boldsymbol{B}}\right)^2}, \tag{44}$$

$$\cos 2\chi = \frac{\left(\hat{\boldsymbol{b}} \cdot \hat{\boldsymbol{B}}\right)^2 - \left(\hat{\boldsymbol{a}} \cdot \hat{\boldsymbol{B}}\right)^2}{\left(\hat{\boldsymbol{a}} \cdot \hat{\boldsymbol{B}}\right)^2 + \left(\hat{\boldsymbol{b}} \cdot \hat{\boldsymbol{B}}\right)^2}. \tag{45}$$

In this frame, the combined redshift and Doppler factor $g \equiv \nu_0/\nu = 1/k^{(t)}$ and $\cos \theta_B = \frac{\hat{k} \cdot \hat{B}}{|\hat{k}||\hat{B}|}$.

2.2.2 Transfer equation

The non-relativistic polarised radiative transfer equation can be written in the form,

$$\frac{\mathrm{d}}{\mathrm{d}s} \begin{pmatrix} I \\ Q \\ U \\ V \end{pmatrix} = \begin{pmatrix} j_I \\ j_Q \\ j_U \\ j_V \end{pmatrix} - \begin{pmatrix} \alpha_I & \alpha_Q & \alpha_U & \alpha_V \\ \alpha_Q & \alpha_I & \rho_V & \rho_U \\ \alpha_U & -\rho_V & \alpha_I & \rho_Q \\ \alpha_V & -\rho_U & -\rho_Q & \alpha_I \end{pmatrix} \begin{pmatrix} I \\ Q \\ U \\ V \end{pmatrix} \tag{46}$$

where (I, Q, U, V) are the Stokes parameters, $j_{I, Q, U, V}$ are the polarised emissivities, $\alpha_{I, Q, U, V}$ are the absorption coefficients, and $\rho_{Q, U, V}$ are the Faraday rotation and conversion coefficients.

In the context of synchrotron radiation, the transfer equation can be simplified by aligning the magnetic field with Stokes U, so that $j_U = \alpha_U = \rho_U = 0$. Then j_Q, α_Q (j_V, α_V) correspond to the emission and absorption coefficients for linear (circular) polarisation and j_I, α_I are the unpolarised coefficients. The transfer coefficients $\rho_{Q, V}$ describe the effects of Faraday conversion and rotation, respectively.

All coefficients are computed in the fluid rest frame, where ν is the emitted frequency, related to the observed frequency through g. Then the transfer equation is recast into invariant form: $\mathsf{I} = g^3 \boldsymbol{I}$, $\mathsf{J} = g^2 \boldsymbol{j}$, and $\mathsf{K} = g^{-1} \mathsf{K}$, where $\boldsymbol{I}$, $\boldsymbol{j}$ and K are the intensity and emissivity vectors and the transfer matrix from equation (46).

Finally, we use the angle χ to rotate the emissivity and absorption matrix in the fluid frame into that of the observer, such that the radiative transfer equation becomes,

$$\frac{\mathrm{d}\mathcal{I}}{\mathrm{d}\lambda} = \hat{\mathsf{J}} - \hat{\mathsf{K}}\mathsf{I}, \tag{47}$$

where λ is an affine parameter, $\hat{\mathsf{J}} = g^2 R(\chi)\boldsymbol{j}$, $\hat{\mathsf{K}} = g^{-1} R(\chi) \mathsf{K} R(-\chi)$, and

$$R(\chi) = \begin{pmatrix} 1 & 0 & 0 & 0 \\ 0 & \cos 2\chi & -\sin 2\chi & 0 \\ 0 & \sin 2\chi & \cos 2\chi & 0 \\ 0 & 0 & 0 & 1 \end{pmatrix}. \tag{48}$$

This rotation transforms the fluid frame polarisation basis to that at infinity, including the parallel transport of the polarisation four-vector along the ray.

Equation (47) includes all relativistic effects. The bending of light is accounted for by the calculation of null geodesics (Dexter & Agol 2009), the gravitational redshifts and Doppler shifts due to fluid motions are included in g.

This method, developed by Shcherbakov & Huang (2011), parallel transports the polarisation basis along the ray and into the fluid frame. This is similar to the approach of Connors et al. (1980),

who transported a local polarisation vector f^μ from the fluid to the observer. Gammie & Leung (2012) derived a general formalism for covariant polarised radiative transfer, and mathematically showed the equivalence of the approach used here and alternative methods used by Broderick & Blandford (2004) and Schnittman & Krolik (2013). We show tests and example problems comparing results from these methods in Section 3.3.

2.3 Transfer coefficients

The transfer coefficients in equation (47) depend in general on the physical properties of the radiating particles. Here we focus specifically on the case of synchrotron radiation appropriate for studying accretion flows at the lowest observed luminosities (e.g. Sgr A*). Adding different emissivities such as bremsstrahlung to GRTRANS would require a straightforward modification of the code.

In addition, the form of the transfer coefficients depends on the underlying electron distribution function. The appropriate forms for thermal and power-law distributions are implemented in the code. More general distribution functions can be built by combining these components (e.g. a thermal distribution with a power law 'tail' or a superposition of thermal distributions, Mao et al. 2016). In these special cases, the integral over the distribution function can be analytically approximated to high accuracy in the ultra-relativistic synchrotron limit (e.g. Mahadevan, Narayan & Yi 1996). The full forms for the transfer coefficients as used in GRTRANS and some of their derivations are given in Appendix A.

In addition to synchrotron coefficients, for test problems with optically thick accretion discs the code uses (colour-corrected) blackbody intensity functions for the disc surface brightness.

2.4 Fluid models

The calculation of transfer coefficients for a particular emission model requires knowledge of the fluid state variables of spacetime coordinates. Depending on the model used, this can include the electron density, magnetic field strength and orientation, and the internal energy density in electrons. In GRTRANS we implement several fluid models from the literature. They are described briefly below, and used as code examples and tests in Section 3.3.

2.4.1 Thin accretion discs

The relativistic version (Page & Thorne 1974) of the standard thin disc solution (Shakura & Sunyaev 1973) for axisymmetric, steady accretion in the equatorial plane is implemented and intended for use with a model for the emergent intensity from the disc (e.g. a blackbody). In this case, the net polarisation is taken to follow the result of electron scattering in a semi-infinite atmosphere (Chandrasekhar 1950; Sobolev 1963) specified relative to the disc normal vector (Section 3.1).

2.4.2 Alternative thin accretion discs

We have also implemented a numerical version of the thin accretion disc problem which inputs a temperature distribution $T(r, \phi)$ in the equatorial plane. One example use of this is for calculating spectra of inhomogeneous (or 'patchy') accretion discs (Dexter & Agol 2011), as used for the polarisation calculations described in Dexter & Quataert (2012).

2.4.3 Spherical accretion flow

A solution of the general relativistic fluid equations for spherically symmetric inflow in the Schwarzschild metric following (Michel 1972; Shapiro 1973a) is implemented. The dominant emission in this case comes from synchrotron radiation (Shapiro 1973b). See Dexter & Agol (2009) for details.

For polarised emission, we take the magnetic field to be purely radial. This is done to check that the resulting linear polarisation sums to zero (since for a camera centred on the black hole there is no preferred direction), and the residual is used as an estimate of the minimum systematic uncertainty in the fractional linear polarisation ($\simeq 0.01$ per cent).

2.4.4 Semi-analytic jet model

Broderick & Loeb (2009) presented a semi-analytic jet model based on stream functions found in force-free simulations. We have implemented this solution numerically on a grid of (r,θ) in Boyer–Lindquist coordinates. To generate our numerical solutions, we solve for the magnetic field and velocity structure analytically using their equations (5)–(13). To get the particle density, we tabulate their function $F(\psi)$ numerically using a separate grid of points with roughly constant $z \simeq r_{\rm fp}$ and varying $\psi = r^{2-2\xi}(1 - \cos\theta)$. This function can then be used to calculate the particle density (their equation 13).

The fluid variable solutions from our method appear identical to what is shown in their fig. 4.

2.4.5 Numerical general relativistic MHD solution

We also use another numerical solution, from the public version of the axisymmetric general relativistic MHD code HARM (Gammie et al. 2003; Noble et al. 2006). Starting from a gas torus in hydrostatic equilibrium threaded with a weak magnetic field, the code evolves the equations of ideal MHD in the Kerr spacetime. The magnetorotational instability (Balbus & Hawley 1991) drives turbulence in the torus and the resulting stresses transport angular momentum outwards, leading to accretion on to the central black hole. Snapshots from these simulations have been used as models of Sgr A* (e.g. Noble et al. 2007; Mościbrodzka et al. 2009).

The images used here as examples are from a single snapshot of a simulation with black hole spin $a = 0.9375$ at $t = 2000GM/c^3$ used for comparison with 3D simulations in Dexter et al. (2010). GRTRANS supports fully time-dependent calculations using a series of such simulation snapshots to e.g. calculate accretion flow movies rather than images. It would also be straightforward to adapt the code to work with updated HARM versions, for example with 3D data or non-ideal MHD.

The fluid variables in these simulations are saved in modified Kerr–Schild coordinates and with arbitrary units which assume $G = c = M = 1$. Calculating radiation from these data in GRTRANS requires converting to Boyer–Lindquist coordinates and to cgs units. The coordinate conversion is done analytically in two steps: from modified to standard Kerr–Schild coordinates (Gammie et al. 2003) and then from Kerr–Schild to Boyer–Lindquist coordinates (e.g. Font, Ibáñez & Papadopoulos 1999). Scaling to cgs units is done by (i) fixing the black hole mass, which sets the length- and time-scales, and (ii) choosing an average accretion rate (or equivalently mass of the initial torus). This procedure is discussed in more detail elsewhere (Schnittman et al. 2006; Noble et al. 2007; Dexter et al. 2010).

Once the unit and coordinate conversions are done, we calculate fluid variables at tabulated geodesic coordinates. For all numerical models, we linearly interpolate from the set of nearest neighbours on the grid for the numerical model. The way this is implemented in the code assumes that the grid is uniformly spaced in some coordinates, and the fluid model must include the transformation from those coordinates to Boyer–Lindquist.

For numerical models it is up to the user whether to account for light travel time along the line of sight. When a fixed snapshot is used, as in the HARM examples shown here, the so-called 'fast-light' approximation is used and light travel times are ignored. To account for this effect, a series of snapshots can be loaded into memory. When interpolating fluid variables to the geodesic coordinates, the nearest neighbour snapshot in time is used as in past work (Dexter et al. 2009). Linear interpolation in time can artificially suppress field strengths when the time separation between snapshots is larger than the coherence time of the magnetic field (Dexter et al. 2010). The geodesic coordinate time at each point along a ray is a sum of the time from the first point calculated at the outer boundary used in the calculation, plus an offset to account for the coordinate time from the camera to the outer boundary. This method for including light travel times is memory intensive for e.g. large 3D simulations where the light travel time across the domain is large compared to the snapshot time spacing. GRTRANS uses OPENMP to share memory between threads to help with this issue.

There are several other models implemented in the code in some form, but which have not been tested. It is straightforward to add new fluid models to the code, e.g. by using existing ones as templates.

2.5 Integration of the polarised radiative transfer equations

From the previous steps, we have transfer coefficients specified at tabulated points along a geodesic which are transformed to relativistic invariant form and aligned with the observed Stokes parameters of the distant observer, accounting for parallel transport along each ray.

The final step is to solve the polarised radiative transfer (equation 48) along the geodesic. In GRTRANS, this is done as a separate step following the calculation of the coordinates of the geodesic. While the ray tracing proceeds backwards from the camera towards the black hole, the integration proceeds outwards. This is done so that we may safely set the initial intensity to zero at some point either where the optical depth is large, or where the geodesic has left the emitting volume. Here we describe one numerical integration method and two quadrature methods that are implemented in GRTRANS for integrating the equations.

These methods can be used for relativistic or non-relativistic problems. For consistency with previous literature, we write the non-relativistic versions of the intensity, absorption matrix, emissivity, and step size along the ray at index k as I_k, K_k, j_k and Δs_k in what follows. In GRTRANS, the relativistic invariants $\mathbf{I}(\lambda_k)$, $\hat{\mathbf{K}}(\lambda_k)$, $\hat{\mathbf{J}}(\lambda_k)$, and $\Delta\lambda_k$ take the place of these quantities.

2.5.1 Numerical integration

The most straightforward method is numerical integration of the radiative transfer equation. The radiative transfer equations can be stiff: the required step size for a converged solution decreases sharply once $\tau \gtrsim 1$, where τ is the optical depth associated with any transfer coefficient.

In order to get a robust solution, we use the ODEPACK routine LSODA (Hindmarsh 1983) to advance the Stokes intensities

between each step tabulated on the geodesic. This algorithm adaptively switches between a predictor-corrector (Adams) method for non-stiff systems, and a BDF method for stiff systems. We find it necessary to restrict the maximum step size allowed in λ, since otherwise a large step can miss the region of interest altogether.

Regions of large optical depth often contribute negligibly to the observed intensity but require a small step size, and so we terminate the integration at a maximum optical depth, $\tau_{\max} = 10$ by default. There are further free parameters in LSODA related to the error tolerance.

The locations sampled by LSODA do not correspond exactly to the points tabulated along the ray. We linearly interpolate the transfer coefficients between tabulated points, even though they are highly nonlinear functions of position along the geodesic. The fluid variables vary more smoothly along the ray, and it would be straightforward but more computationally expensive to instead re-interpolate the fluid variables to the points used by LSODA and then calculate new transfer coefficients, as was done in the previous version of the code (Dexter 2011). Given the results from comparing to quadrature integration methods and analytic solutions described below, and from the convergence properties with increasing the number of points along each ray, we find the current approximation adequate for obtaining accurate solutions.

2.5.2 Quadrature solutions

The polarised radiative transfer equations are linear and ordinary, and so admit a formal solution analogous to that of the unpolarised case (Rybicki & Lightman 1979). The solution amounts to finding the matrix operator $\mathbf{O}(s, s')$, defined by (Landi Degl'Innocenti & Landi Degl'Innocenti 1985),

$$\frac{\mathrm{d}}{\mathrm{d}s}\mathbf{O}(s, s') = -\mathbf{K}(s)\mathbf{O}(s, s'), \tag{49}$$

$$\mathbf{O}(s, s) = \mathbf{1}, \tag{50}$$

which determines how the intensity is propagated over some part of the ray in the absence of emission. In the unpolarised case this is a scalar, $O = \exp[-(\tau(s) - \tau(s'))]$. If the absorption matrix $\mathbf{K}$ is a constant over the ray, then similarly,

$$\mathbf{O}(s, s') = \exp[-\mathbf{K}(s - s')]. \tag{51}$$

In terms of $\mathbf{O}$, the intensity can be written in terms of an initial value $I_{n-1}(s_{n-1})$:

$$\mathbf{I}(s) = \int_{s_{n-1}}^{s} \mathrm{d}s'\mathbf{O}(s, s')j(s') + \mathbf{O}(s, s_{n-1})I_{n-1}. \tag{52}$$

Landi Degl'Innocenti & Landi Degl'Innocenti (1985) found a closed form solution for $\mathbf{O}$ (their equation 10, reproduced in Appendix D). This solution is valid for regions where the transfer matrix $\mathbf{K}$ is constant, but not for our situation of interest where they vary arbitrarily along a ray. In order to use this expression, we assume that the coefficients are constant in between the tabulated locations along a geodesic starting from $s_{k=n}$ at the farthest point of interest along the ray (at the black hole or where the ray leaves the far end of the emitting region) and integrating towards $s_{k=0}$ (the 'surface'), and write the solution of equation (52) separately for the interval between neighbouring points with indices $k + 1$ and k with positions s_{k+1} and s_k:

$$I_k = O_{k,k+1}j_k\Delta s_k + O_{k,k+1}I_{k+1}, \tag{53}$$

where $\Delta s_k = s_{k+1} - s_k$. This formula is used recursively going outwards from s_{n-1} to s_0 to find the intensity everywhere from the initial condition $I_{n-1} = 0$.

The final integration method implemented in GRTRANS is the diagonal element lambda operator method (DELO; Rees, Durrant & Murphy 1989), which comes from writing the transfer equations in terms of the unpolarised optical depth, $\mathrm{d}\tau = \alpha_I\mathrm{d}s$, and the modified absorption matrix $\mathbf{K}' = \mathbf{K}/\alpha_I - \mathbf{1}$ and source function $S' = \mathbf{j}/\alpha_I$:

$$\frac{\mathrm{d}\mathbf{I}}{\mathrm{d}\tau} = \mathbf{I} - \mathcal{S}, \tag{54}$$

where $\mathcal{S} = S' - \mathbf{K}'\mathbf{I}$. This equation has a formal solution between neighbouring points τ_{k+1}, τ_k of

$$I(\tau_k) = E_k I(\tau_{k+1}) + \int_{\tau_k}^{\tau_{k+1}} \exp[-(\tau - \tau_k)]\mathcal{S}\mathrm{d}\tau, \tag{55}$$

where $E_k = \exp(-\delta_k)$ and $\delta_k = \tau_{k+1} - \tau_k$. The DELO method makes a linear approximation for the modified source function,

$$\mathcal{S}(\tau) = [(\tau_{k+1} - \tau)\mathcal{S}_k + (\tau - \tau_k)\mathcal{S}_{k+1}]/\delta_k, \tag{56}$$

so that equation (56) can be integrated analytically between grid points, giving:

$$I(\tau_k) = \mathcal{P}_k + \mathcal{Q}_k I(\tau_{k+1}), \tag{57}$$

where

$$\mathcal{P}_k = \mathcal{M}_k \left[(F_k - G_k)S'_k + G_k S'_{k+1}\right], \tag{58}$$

$$\mathcal{Q}_k = \mathcal{M}_k \left(E_k\mathbf{1} - G_k K'_{k+1}\right), \tag{59}$$

$$\mathcal{M}_k = \left[\mathbf{1} + (F_k - G_k)K'_k\right]^{-1}, \tag{60}$$

$$F_k = 1 - E_k, \tag{61}$$

$$G_k = [1 - (1 + \delta_k) E_k]/\delta_k. \tag{62}$$

The difficulty with this method is that τ_k is used as the independent variable. For our problems of interest τ can be nearly constant between grid points over which the fluid quantities and emissivity change significantly, which causes the above solution to fail. In the limit of small δ_k, we instead expand the above quantities up to $\mathcal{O}(\delta_k^2)$, leading to the following forms:

$$\mathcal{P}_k = \mathcal{M}_k \left[\frac{j_k\Delta s_k}{2} - \frac{\Delta s_k^2\alpha_{I,k}j_k}{6} + \frac{j_{k+1}\Delta s_k}{2}\right. \tag{63}$$

$$\left. - \frac{\Delta s_k^2\alpha_{I,k}j_{k+1}}{3}\right], \tag{64}$$

$$\mathcal{Q}_k = \mathcal{M}_k \left[\mathbf{1}\left(1 - \frac{\Delta s_k\alpha_{I,k}}{2} + \frac{\Delta s_k^2\alpha_{I,k+1}^2}{6}\right)\right. \tag{65}$$

$$\left. - \left(\frac{\Delta s_k}{2} - \frac{\Delta s_k^2}{3}\right) K_{k+1}\right], \tag{66}$$

$$\mathcal{M}_k = \left[\left(1 - \frac{\delta_k}{2} + \frac{\delta_k^2}{6}\right)\mathbf{1}\right]^{-1}. \tag{67}$$

This version of the equations uses s as the independent variable, and is used by default when $\delta_k < 10^{-2}$. Since the number of steps taken by GRTRANS is usually $\gtrsim 400$, this form of the equations is used unless the optical depth is very large.

In GRTRANS, all integration methods proceed outwards from an initial point back towards the camera. From the recursive forms of the DELO and formal solution methods, we see that it would also be possible to integrate the polarised radiative transfer equations backwards by summing the so-called contribution vectors from each point to the final intensity on the camera, I_0:

$$I_0 = \Sigma_{i=0}^{n-1} \mathcal{C}_i, \tag{68}$$

where

$$\mathcal{C}_i = \left[\Pi_{m=0}^{i-1} O_{m,m+1} \right] j_i \tag{69}$$

for the formal solution method and

$$\mathcal{C}_i = \left[\Pi_{m=0}^{i-1} \mathcal{Q}_m \right] j_i \tag{70}$$

for the DELO method (Rees et al. 1989). The equivalent contribution vectors in the unpolarised case are given as

$$\mathcal{C}_i = \left[\Pi_{m=0}^{i-1} e^{-(\tau_{m+1}-\tau_m)} \right] j_i = e^{-\tau_i} j_i, \tag{71}$$

where τ_i is the optical depth from the surface to the depth at index i.

Tracing backwards from the camera, at each step at index i one can calculate $\mathcal{C}_i$ using the solution for $\mathcal{C}_{i-1}$, K_i, and j_i. Solving the polarised radiative transfer equations in this way would be useful in implementations where the geodesic equations and radiative transfer equations are solved simultaneously, e.g. as is done for the unpolarised case in the public code GYOTO (Vincent et al. 2011). In this method, one can then safely terminate the integration early if the product term in $\mathcal{C}_i$ becomes sufficiently small (e.g. the optical depth becomes large).

The three methods give consistent answers, usually to high accuracy and with similar performance. The main drawback of our quadrature implementations is the lack of an adaptive step size, so that many steps ($\sim 10^3$) are required in order to get a converged result. In most example problems in the following section, the numerical integrator is used as it is the most robust choice. The other methods are primarily used for comparison and testing, although they are faster at a fixed number of points n and so with some optimisation might prove to be significantly faster than numerical integration.

3 TESTS AND EXAMPLES

Here we describe tests of the different aspects of GRTRANS (unit tests), as well as full example problems which are compared with results from the literature. We do not provide tests of the GEOKERR code for calculating null geodesics in the Kerr metric, which are described in Dexter & Agol (2009).

3.1 Parallel transport tests

The accuracy of the method for the parallel transport of a vector in the Kerr metric can be checked by calculating the Penrose–Walker constant at each point along the ray, compared to the value at the camera. In GRTRANS, this value remains constant along the ray to machine precision. This result is expected, since the parallel transport in the Kerr metric is done analytically (Section 2.2).

The transported polarisation basis is compared to the polarisation basis of the emission at each point in the so-called comoving orthonormal frame (Shcherbakov & Huang 2011), where the fluid four-velocity $u^\mu = (-1, 0, 0, 0)$. We can verify that this transformation is done correctly in several ways. First, we can check that

$u^\mu = (-1, 0, 0, 0)$ after the transformation is done. This is the case to the same precision that $u^\mu u_\mu = -1$ in the coordinate frame. For analytic models, the agreement is to machine precision. For numerical models like FFJET and HARM, there can be errors of $\sim 10^{-3}$ from interpolating the four-velocity to the geodesic coordinates.

Additional tests of the frame transformation come from comparing the combined redshift Doppler shift factor g found from $1/k^t$ to that obtained from the analytic expression for this quantity in equation (16) of Viergutz (1993). A comparison for a sample geodesic from the numerically implemented FFJET model is shown in the left-hand panel of Fig. 1. In the right-hand panel of Fig. 1 we compare the angle between k^μ and b^μ in the orthonormal fluid frame to the covariant method for computing the same angle from Broderick (2004):

$$\cos^2 \theta_B = \frac{(b^\mu k_\mu)^2}{b^\nu b_\nu [k^\sigma k_\sigma + (k^\rho u_\rho)^2]}, \tag{72}$$

where here $k^\sigma k_\sigma = 0$ for geodesics. The agreement is excellent for both quantities, with significant deviations only appearing in θ_B when $k^\mu b_\mu$ is very small. These deviations are again a result of interpolating the magnetic field and velocity four-vectors, and are systematic errors in any calculation involving numerical fluid data.

We use the method of Shcherbakov & Huang (2011) to project the local polarisation basis in the fluid on to that of the parallel transported polarisation basis of the observer. Connors et al. (1980) and Agol (1997) used a similar method, but instead parallel transported local vectors orthogonal and parallel to an accretion disc in the equatorial plane and k^μ to the distant observer. For our purposes, we want the orthogonal vector, which is given in Boyer–Lindquist coordinates as (Agol 1997),

$$f_\perp^t = 0, \tag{73}$$

$$f_\perp^r = \frac{\sqrt{\Delta} k^{(\theta)} k^{(r)}}{r N_f}, \tag{74}$$

$$f_\perp^\theta = \frac{1}{r N_f} \left[k^{(r)^2} + (1 + v^2) k^{(\phi)^2} - 2v k^{(\phi)} k^{(t)} \right. \tag{75}$$

$$\left. + v k^{(\theta)^2} k^{(\phi)} / k^{(t)} \right], \tag{76}$$

$$f_\perp^\phi = \frac{r k^{(\theta)}}{\sqrt{A} N_f} \left[-(1 + v^2) k^{(\phi)} + v k^{(t)} \right. \tag{77}$$

$$\left. + v k^{(\phi)^2} / k^{(t)} \right], \tag{78}$$

where $k^{(\mu)}$ are the components of k^μ in the locally non-rotating frame (Bardeen et al. 1972) and N_f is a normalization chosen so that $f_\perp^\mu f_{\mu,\perp} = 1$. The polarisation angle ψ is then given in terms of K_1 and K_2 [equation (3)]:

$$\tan \psi = \frac{-K_1 \beta - K_2 \gamma}{K_2 \beta - K_1 \gamma}. \tag{79}$$

We can directly compare this to the rotation angle χ from equation (44), as long as we identify b^μ, used in GRTRANS as the polarisation reference vector, with their disc normal vector, $f_\perp^\mu$ above. A comparison between our angle χ and their ψ is shown in Fig. 2 for polarisation from electron scattering in a thin accretion disc. The
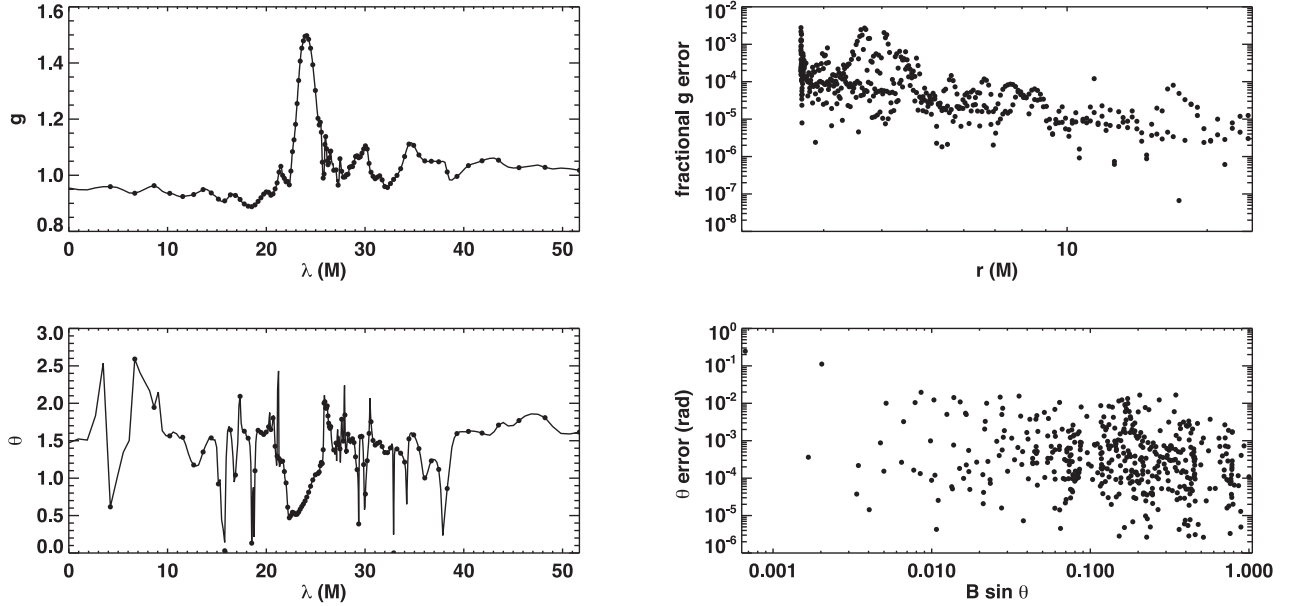
Figure 1. Comparison between redshift/Doppler factor g from Viergutz (1993) and fluid frame angle between k^μ and b^μ from Broderick (2004) calculated in terms of coordinate frame quantities, and the same quantities calculated in the orthonormal fluid frame (section 2.2, Shcherbakov & Huang 2011) for a sample geodesic using the numerical FFJET model. The residuals give an idea for the systematic errors in these quantities, usually <1 per cent, which arise from interpolating the four-velocity. The error in θ_B can be large when $k^\mu b_\mu$ is very small, but here the synchrotron emissivity is also small. For clarity, only one of every four points is plotted.
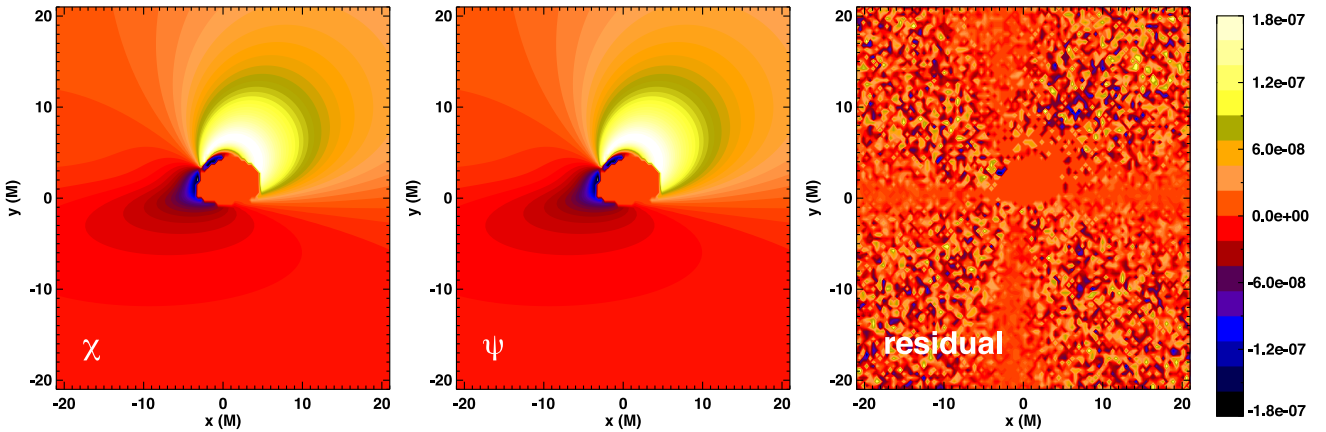
Figure 2. The rotation element $\sin 2\chi$ relating the Stokes parameters measured at the camera to those locally measured relative to lie in the plane of the disc. The left-hand panel shows this quantity calculated by parallel propagation of the camera back to the disc (Shcherbakov & Huang 2011, and Section 2.2) while the centre panel is calculated by parallel transporting the local polarisation vector to the camera (Connors et al. 1980; Agol 1997). In both cases the colours scale linearly from -1 (blue) to 0 (red) to $+1$ (white). The residuals (right-hand panel and colour bar) show that the two methods agree to machine single precision.

agreement is to machine single precision, as previously found by Schnittman & Krolik (2013).

These comparisons verify both sets of methods used for calculating redshift/Doppler factors, and angles between the magnetic field and wave vectors and between the polarisation basis in the fluid frame and that of the observer, accounting for parallel transport along the ray. The residual systematic errors <1 per cent in these quantities, are comparable to or smaller than the level of accuracy achieved in other parts of the calculation (e.g. the integration or the transfer coefficients).

3.2 Integration tests

We test the accuracy and precision of the different methods for integrating the polarised radiative transfer equations given in Section 2.5 through comparison to idealized, analytic solutions with constant coefficients along a ray. We consider two test problems, one for each limiting regime of the equations. The first problem uses only emission and absorption in Stokes I,Q. The analytic solution is given in equation (C2), and a comparison of the analytic solution and that calculated using the LSODA integration method is shown in Fig. 3. The agreement is excellent to within single precision.
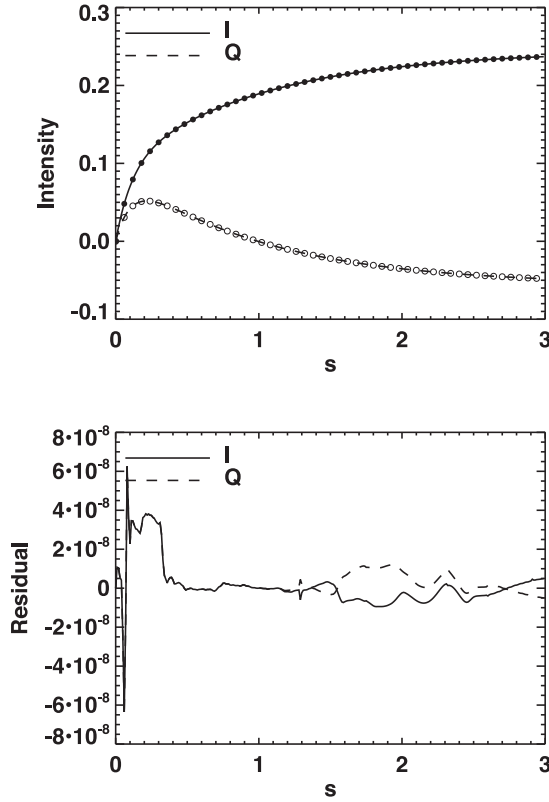
Figure 3. Analytic (lines) and numerical GRTRANS (dots) solutions to the polarised emission and absorption test problem (see Section 3.2, Appendix C) for the Stokes parameters *I* and *Q*. Single precision accuracy is maintained over the entire ray.

Figure 4. Analytic (lines) and numerical GRTRANS (dots) solutions to the intrinsic Faraday rotation and conversion test problem (see Section 3.2, Appendix C) for the Stokes parameters *Q*, *U*, and *V*. The residuals in this case grow along the ray. However, the absolute error remains small unless a very large number of oscillations are present.

The second problem is the intensity in Stokes *Q*, *U*, *V* for pure Faraday rotation and conversion (ρ_V and ρ_Q) with emission in *Q* and *V*. The analytic solution is purely oscillatory, and is given in equation (C5). Again the agreement between analytic and numerical solutions is excellent (Fig. 4). In this case the residuals grow with each oscillation. Still, the absolute errors are so small that the error will be negligible unless the Faraday optical depth is enormous, in which case code convergence and run time will also become poor. This is not a limit of interest here, but the issue and some possible solutions are discussed in Shcherbakov et al. (2012).

3.3 Test problems

Finally we show examples of full test problems based on calculations in the literature. The first example is of the total intensity and linear polarisation of a relativistic, thin accretion disc (Page & Thorne 1974) in the equatorial plane. The emission is assumed to be optically thick so that the emergent intensity from each point on the disc is a blackbody at the local photospheric temperature. The emergent polarisation is from electron scattering from a semi-infinite slab (Chandrasekhar 1950; Sobolev 1963). Fig. 5 shows the resulting total intensity, on a log scale, and polarisation vectors. The parameters are $M = 10M_\odot$, $\dot{M} = 0.1\dot{M}_{Edd}$, and the image is integrated over X-ray energies $0.1 - 10$ keV. The results are in excellent agreement with fig. 1 of Schnittman & Krolik (2009).

Next we calculate polarised synchrotron radiation from the semi-analytic jet model of Broderick & Loeb (2009). The calculation of the jet structure is described there and in Section 2.4.4. The
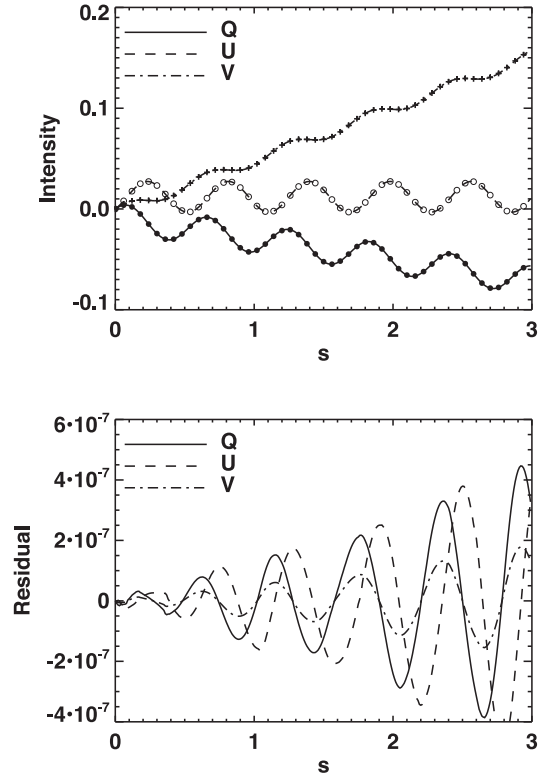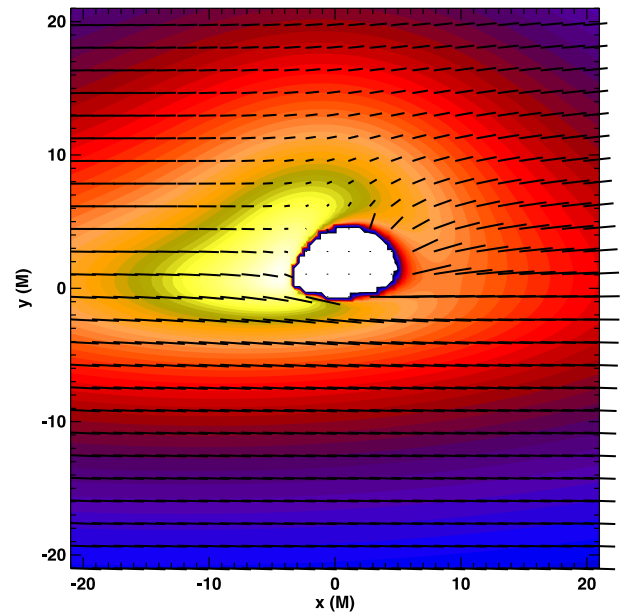

Figure 5. Intensity and linear polarisation map of thermal emission from a thin accretion disc, ignoring the effect of returning radiation (Agol & Krolik 2000). The intrinsic polarisation is assumed to follow the solution for scattering in a semi-infinite atmosphere (Chandrasekhar 1950; Sobolev 1963). The black hole mass is $10M_\odot$, the accretion rate is $0.1\dot{M}_{edd}$, and the inclination angle is $\theta_0 = 75°$. The image is log-scaled with a colour scale chosen to match fig. 1 of Schnittman & Krolik (2009). Both the total intensity and polarisation results are in excellent agreement with theirs.
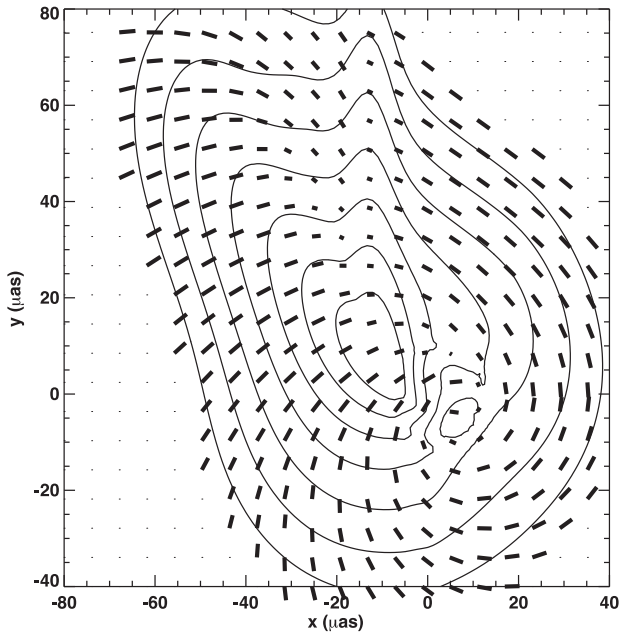
Figure 6. Total intensity (contours) and linear polarisation map from the semi-analytic jet model of Broderick & Loeb (2009). The parameters are $a = 0.998$, $\xi = 0.5$, $i = 25°$, $\nu_0 = 345$ GHz. The results are mostly in good agreement with those of their M0 model (Fig. 7). The discrepancies arise in the counter-jet, which contains little of the total or polarised flux.

electrons in the jet are assumed to follow a power-law distribution with a minimum Lorentz factor of 100. Our transfer coefficients for this case are different than theirs, since we account for the cut off of the distribution function at low energies (see Appendix A). The resulting total intensity and polarisation are shown in Fig. 6, and are for the most part in good agreement with those of their M0 model in their fig. 7. The discrepancies are only in the polarisation structure of the counter-jet (bottom right of the image), which could be from differences in how the jet solution is reflected across the plane $z = 0$. In any event that region of the image contains little total or polarised flux.
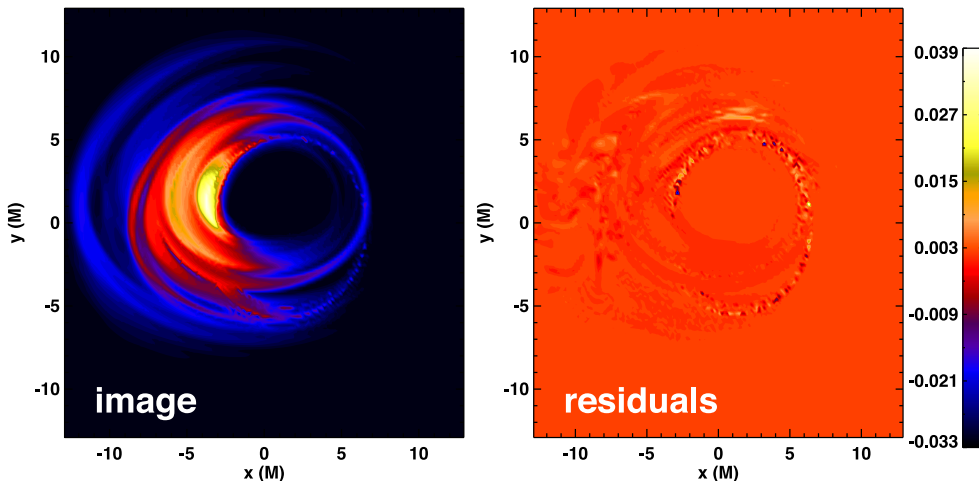
We can also compare the total intensity image from a relativistic MHD simulation between the previous (Dexter 2011; Dexter et al. 2012a) and new versions of the GRTRANS code (Fig. 7). The simulation used the public version of the HARM code (Gammie et al. 2003; Noble et al. 2006) with a black hole spin of $a = 0.9375$. The simulation results have been scaled to model the submillimetre emission of Sagittarius A*, with a mean electron temperature in the inner disc $\simeq 5 \times 10^{10}$ K and an accretion rate chosen so that the flux at $\nu = 230$ GHz is roughly $F_\nu \simeq 3$ Jy. The agreement between two independent versions of the code is excellent (maximum pixel residuals $\simeq 4$ per cent and total flux residual $\simeq 0.3$ per cent). The previous version used the alternative methods for finding θ_B and g described in Section 3.1, as well as a quadrature method for the intensity. That code version also interpolated the fluid variables rather than the emission and absorption coefficients. The residuals show that the systematic errors from these different methods lead to only small difference in the resulting total intensity image in a representative case.

As a final example, we show images and polarisation maps from the HARM fluid model in Fig. 8 with parameters chosen to model the submm bump in Sgr A* (e.g. Mościbrodzka et al. 2009; Dexter et al. 2010). The top left panel includes all absorption and transfer effects. Including the Faraday effects in particular leads to significant rotation of the polarisation vectors and depolarisation, in contrast to some previous results finding coherent polarisation structures (e.g. Bromley, Melia & Liu 2001; Broderick & Loeb 2006) when Faraday effects were ignored. The Faraday effects arise within the emission region itself, even though the electrons are mildly relativistic ($\theta_e \sim 10$).

We can understand this result in terms of known expressions for the transfer coefficients (Appendix B). The typical ratio ν/ν_c for these types of Sgr A* models in the submm is:

$$\frac{\nu}{\nu_c} \simeq 40 \left(\frac{B}{30\text{G}} \right)^{-1} \left(\frac{\theta_e}{10} \right)^{-2} \left(\frac{\nu}{230 \text{ GHz}} \right). \tag{80}$$

At this value, for moderately relativistic temperatures the Faraday coefficients can be much larger than the total absorption coefficient (Fig. B1). Jones & Hardee (1979) argued that because this is only true when $\nu/\nu_c \gg 1$ where absorption is typically negligible, Faraday rotation and conversion would be negligible in thermal
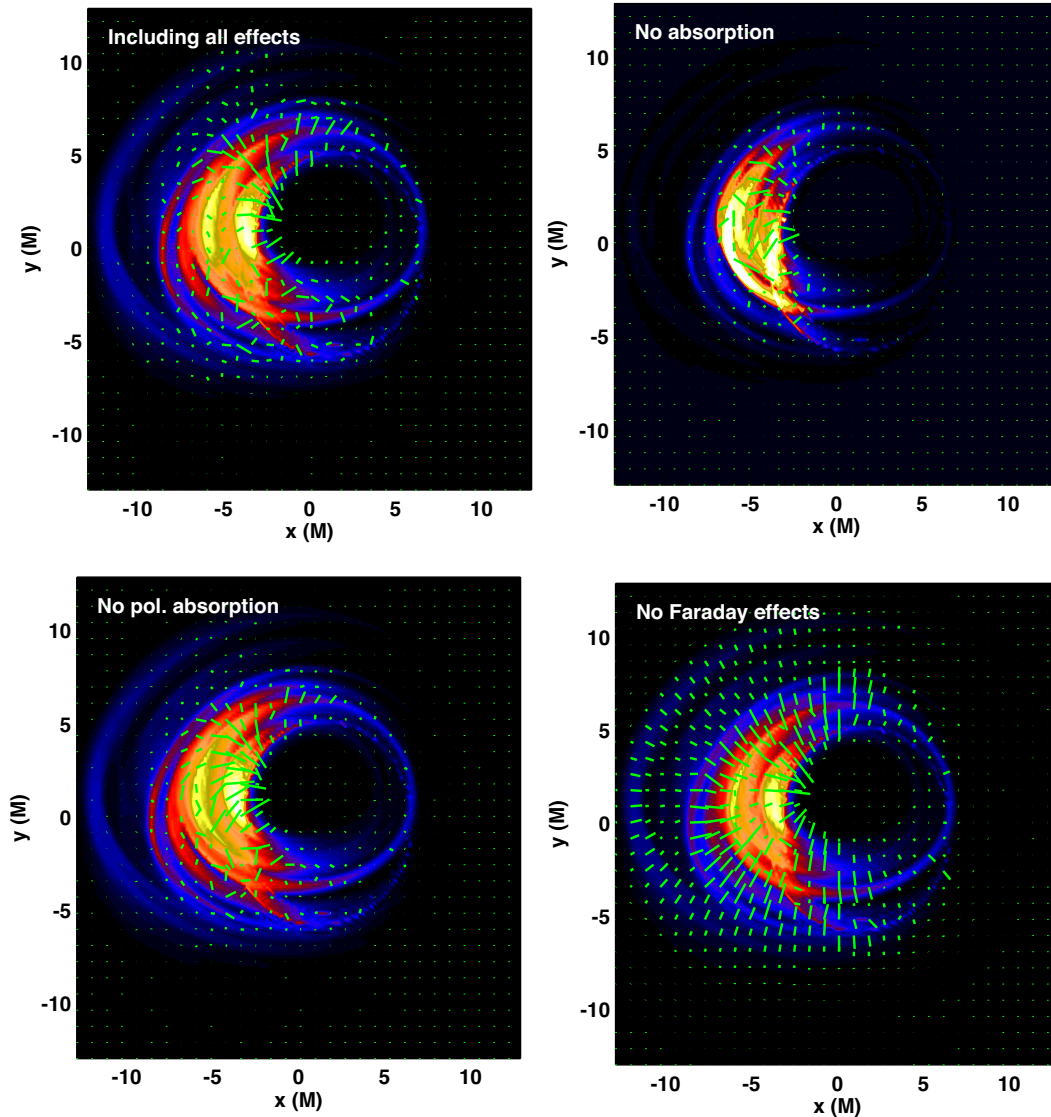

Figure 7. Total intensity false colour image of synchrotron radiation from a GRMHD simulation generated with the HARM code from the current version of GRTRANS, and the residuals between the current and previous versions of the code relative to the maximum overall image intensity. Only one image is shown, since they appear indistinguishable. The two code versions use different methods for handling Doppler beaming, gravitational redshifts, and the integration of the radiative transfer equation. The agreement is excellent between the two cases: the largest intensity residuals are ~4 per cent of the maximum, and the total flux agrees to $\simeq 0.3$ per cent.

Figure 8. Images and linear polarisation maps of Sgr A* corresponding to the HARM test problem. The top left image includes the full set of absorption and rotation coefficients. In each of the other panels, one or more of these coefficients are ignored to show their different effects on the total intensity and linear polarisation structure. Comparing the top left and bottom right images, for example, shows that intrinsic Faraday rotation is responsible for significantly depolarising the resulting image. The polarised absorption components play an important role in suppressing the polarisation in the brightest regions of the image (bottom left). The top right panel shows that self-absorption plays an important role in suppressing the total and polarised flux.

plasmas. However, the submm bump in Sgr A* is likely still marginally self-absorbed (e.g. Falcke et al. 1998; Bower et al. 2015). This is certainly the case for these model images, where the image is significantly modified in the top right panel when absorption is neglected. In these models, the effective optical depth from Faraday effects $\tau = \rho_{Q,V} R \lesssim 100$ and therefore significantly modifies the polarisation structure. Since Faraday effects are sensitive to ν/ν_c and θ_e, the measured coherence of the spatially resolved polarisation structure (e.g. Johnson et al. 2015) provides constraints on these quantities and in turn on the properties of the emitting plasma.

The polarised absorption coefficients also play a role in limiting the polarisation fraction of the brightest pixels of the image (comparing the top left and bottom left panels), but including these components does not have a significant impact on the total intensity image. Images of Sgr A* from previous calculations using only total intensity radiative transfer are then unlikely to be subject to systematic errors from neglecting these coefficients.

4 CODE STRUCTURE AND PERFORMANCE

In this section we describe the accuracy, convergence, performance, and scaling of GRTRANS, and then provide a brief overview of its organization.

4.1 Convergence

The accuracy of GRTRANS is very high for smooth solutions (e.g. Section 3.2), where the coefficients are tabulated over much shorter sections of the ray than the intensity changes appreciably. However, in problems of interest for ray tracing, the emission and absorption coefficients generally change rapidly along the ray, especially in the case of synchrotron radiation where they are strong functions of the fluid state variables. In these cases the rays will generally be sampled sparsely compared to the scale over which the coefficients change. Then the accuracy scales roughly linearly with the number
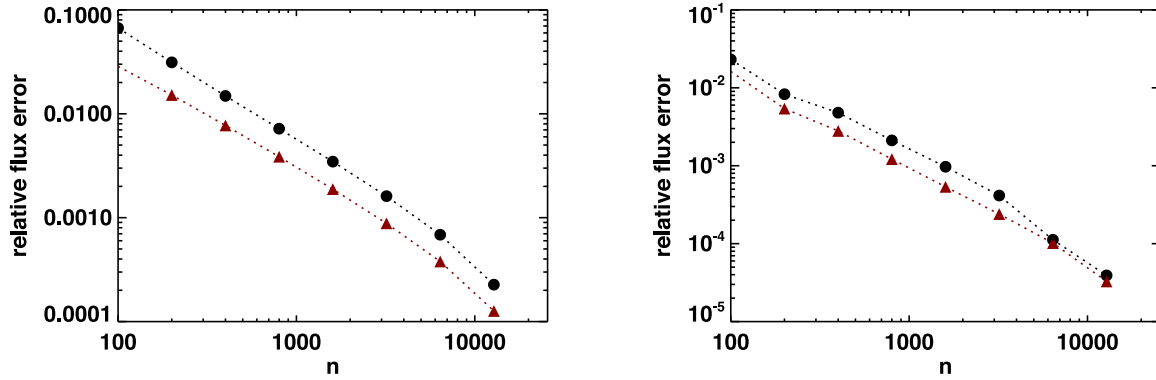
Figure 9. Convergence of the total image flux as a function of the number of points tabulated along each geodesic for the M87 semi-analytic jet (left) and HARM Sgr A* (right) test problems with full polarisation using numerical (black circles) or quadrature (red triangles, equation 54) integration methods. The convergence is roughly linear with n, $\Delta F/F \sim 10^{-2}(n/400)^{-1}$, where the normalization of the error varies at order unity between different problems of interest, camera sizes, and integration methods.

of points along each geodesic, and a sufficient number of points must be chosen to reach the desired accuracy.

Fig. 9 shows the convergence of the total flux in the solutions to the HARM and semi-analytic jet problems as a function of n, compared to the solution with $n = 25600$. For typical problems of interest, the precision is better than ~ 1 per cent $(n/400)^{-1}$. The precision is also usually better for the numerical integration method than the formal solution method, although there are cases where the reverse is true (bottom panel Fig. 9). In most applications, $n > = 400$ should ensure that systematic errors elsewhere in the code (e.g. in the approximations to the synchrotron emissivities) would dominate the total error budget. There is no sign of systematic disagreement between the two integration methods. With $n = 25\,600$, their total fluxes agree to 0.01 per cent, consistent with the linear convergence of each method.

4.2 Performance and scaling

The calculation of the intensity at each camera pixel in ray tracing are independent, and as such it is possible to speed up calculations considerably on multicore machines by assigning different parts of the calculation to different cores. This is achieved simply in GRTRANS by using different OPENMP threads for different sets of camera pixels. Although there is overhead associated with creating and destroying threads, the efficiency is still high (>80 per cent in all problems and on all systems studied), and with the added benefit that memory can be shared by all threads, an important benefit for e.g. the post-processing of high resolution 3D MHD simulations. Alternatively, threads could be used at the level of different images, which might improve the efficiency, but would then provide no speed up for calculating single images.

Fig. 10 shows a strong scaling test for GRTRANS using the spherical accretion example problem. The wall time taken by the parallel part of the code is measured as a function of the number of OPENMP threads on a 24-core workstation. The points are the measured times from single instances of running the code, while the solid line is perfect scaling relative to the measured run time using a single core. The efficiency for this problem peaks at 48 threads (2 threads/core or 1 thread/hyperthread), and is $80 - 100$ per cent for different values of n. These results are typical for a wide range of test problems.
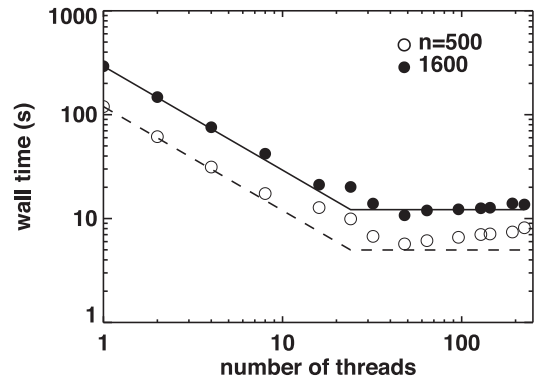

Figure 10. Strong scaling test of the GRTRANS code using the spherical accretion test problem. The wall time for single runs of the code with $n = 500$ (open dots), 1600 (solid dots) is plotted versus the number of threads used on a 24-core machine (two 12 core processors). The lines show 100 per cent scaling for the machine based on the execution time for a single thread. The peak efficiency of $\simeq 80 - 100$ per cent for this problem is reached using 2 threads/core. The efficiency exceeds 100 per cent for 48 threads in the $n = 1600$ case, either due to run to run variability or improved performance when hyperthreading is in use. The performance range found here also applies to all other problems tested so far, and does not seem to depend on the total number of cores or processors used.

4.3 Code organization

The calculation of radiative transfer around a spinning black hole consists of several independent pieces. In order to maintain flexibility, each of these aspects of the calculation is implemented as a separate FORTRAN 90 module in GRTRANS. This Section describes the different modules and how they are used together to run GRTRANS. More detailed information about the code, explicit examples of its use, and guidelines for adding new fluid and emission models are included in the code distribution.

4.3.1 Kerr null geodesic calculation

Rays in GRTRANS are assumed to be null geodesics in a Kerr space-time, and their trajectories in Boyer–Lindquist coordinates are calculated using the semi-analytic public code GEOKERR (Dexter & Agol 2009). In addition to the existing public FORTRAN interfaces

for GEOKERR, there is now also a public PYTHON interface to GEOKERR compiled using f2py.

The version of GEOKERR used by GRTRANS includes a few minor bug fixes from the release version. The most important bug fix is that the option to use $\mu = \cos\theta$ as an independent variable now works robustly even when many turning points are present in a short segment of the orbit. A bug associated with failures in the ϕ and t coordinates in rare cases where a ray is sampled extremely close to a turning point has also been fixed.

4.3.2 Fluid models

GRTRANS is designed to work with a range of models describing the state variables of gas in the Kerr spacetime, from non-relativistic semi-analytic solutions to the fluid equations (e.g. Yuan, Quataert & Narayan 2003; Broderick et al. 2009; Broderick & Loeb 2009) to numerical solutions specified on a tabulated grid. These fluid models are implemented separately, one per file, each of which contains a common set of routines to initialize the model (including allocating data), calculate fluid state variables at Boyer–Lindquist coordinate positions in the Kerr metric, and delete the model (including deallocating data). The code currently has several such models implemented as are used in the example problems here. It is straightforward to add new fluid models for use with the code using these existing models as templates.

Since the fluid models are implemented separately, they can be used independently of GRTRANS. This is useful for testing that the implementation is correct. Examples in the code are included also for using f2py to build PYTHON interfaces to such models, so that their results can be accessed from PYTHON.

4.3.3 Transfer coefficients

In general, the calculation of the transfer coefficients is handled independently of the fluid model. The emission models included at present are synchrotron emission from thermal or power-law particle distributions and optically thick colour-corrected blackbody radiation, which can also include linear polarisation induced from electron scattering in a semi-infinite atmosphere.

As with fluid models, the user can include new emission models by using the existing ones as templates. It is also straightforward to combine various emissivities by writing a new one which then calls combinations of those already in use. Examples of this included in the code are the HYBRID and MAXJUTT emissivities, which are combinations of synchrotron emission from thermal+PL and multiple thermal with different temperatures (see Mao et al. 2016, for details).

The synchrotron emissivities can be compiled with f2py and used directly from PYTHON.

4.3.4 Other modules

Many routines associated with the Kerr metric, including the implementation of the method for parallel transport of vectors along geodesics, are stored in their own module. The integration methods for the radiative transfer equation are as well, and also include an f2py interface for use in PYTHON.

4.3.5 GRTRANS driver routine

The main driver routine calculates the intensity at a specified number of observed frequencies and values of other parameters (e.g. mass accretion rate) for a given set of inputs.

The driver routine has global objects associated with the above geodesic, fluid, emissivity, and radiative transfer modules. These are used to store inputs and data. The objects are global so that they can be accessed from the LSODA integration routines.

4.3.6 PYTHON interface

A python class for GRTRANS includes all of the code inputs and methods for reading the output. There are two main interfaces to the code, either through the use of FORTRAN input files (namelists) or through the PYTHON wrapper to the code, which compiles with f2py. Both interfaces can be used with PYTHON, while the code can also be run from the command line using input files.

5 DISCUSSION

We have developed a new public code, GRTRANS, for polarised ray tracing radiative transfer calculations in the Kerr metric, designed with applications to modelling the emission from low-luminosity black holes in mind. For this reason the code is currently focused on synchrotron radiation (Appendix A), and is written to work with a wide range of underlying models for the accreting or outflowing gas, from semi-analytic models (e.g. spherical accretion or force-free jets) to relativistic MHD simulations (e.g. HARM). The code is intended to be modular, so that it is straightforward to add new fluid or emission models. It is written in FORTRAN to make use of previous work on null geodesics and other routines, but can be used efficiently from PYTHON. We have quantitatively compared results for independent methods for parallel transport and integrating the polarised radiative transfer equations in an effort to verify the code, and presented full examples of comparisons with published work.

The code is written to do ray tracing in the Kerr metric, and as such has two major limitations. First, many aspects of the code assume that the background spacetime is the Kerr metric (e.g. the null geodesic calculation in GEOKERR and the parallel transport method). Generalizing to other spacetimes is possible but would require major changes to the code. The public GYOTO code (Vincent et al. 2011) would probably be a better option for ray tracing in a wide range of spacetimes, although at the moment it does not include polarised radiative transfer. Second, ray tracing assumes that the photon trajectories are known a priori, and so is impractical for calculations where Compton scattering is important but where the total Compton optical depth is small. In this case, one could approximate the scattering locally, or do a first calculation to estimate the effective emission/absorption from scattering. Still, Monte Carlo methods such as those used in GRMONTY (Dolence et al. 2009) or PANDURATA (Schnittman & Krolik 2013) may be better suited to such problems.

ACKNOWLEDGEMENTS

REFERENCES

Abramowitz M., Stegun I. A., 1970, Handbook of Mathematical Functions: With Formulas, Graphs, and Mathematical Tables

Agol E., 1997, PhD thesis, University of California, Santa Barbara

Agol E., Krolik J. H., 2000, ApJ, 528, 161

Akiyama K. et al., 2015, ApJ, 807, 150

Balbus S. A., Hawley J. F., 1991, ApJ, 376, 214

Bardeen J. M., Press W. H., Teukolsky S. A., 1972, ApJ, 178, 347

Beckwith K., Hawley J. F., Krolik J. H., 2008, MNRAS, 390, 21

Blumenthal G. R., Gould R. J., 1970, Rev. Mod. Phys., 42, 237

Bower G. C. et al., 2015, ApJ, 802, 69

Broderick A. E., 2004, PhD thesis, California Institute of Technology, California, USA

Broderick A., Blandford R., 2004, MNRAS, 349, 994

Broderick A. E., Loeb A., 2005, MNRAS, 363, 353

Broderick A. E., Loeb A., 2006, ApJ, 636, L109

Broderick A. E., Loeb A., 2009, ApJ, 697, 1164

Broderick A. E., Fish V. L., Doeleman S. S., Loeb A., 2009, ApJ, 697, 45

Bromley B. C., Melia F., Liu S., 2001, ApJ, 555, L83

Chandrasekhar S., 1950, Radiative Transfer, Clarendon Press, Oxford

Chandrasekhar S., 1983, The Mathematical Theory of Black Holes, Clarendon Press/Oxford Univ. Press, Oxford/New York

Chan C.-K., Psaltis D., Özel F., Narayan R., Sąowski A., 2015, ApJ, 799, 1

Chen B., Kantowski R., Dai X., Baron E., Maddumage P., 2015, ApJS, 218, 4

Connors P. A., Stark R. F., 1977, Nature, 269, 128

Connors P. A., Stark R. F., Piran T., 1980, ApJ, 235, 224

Cunningham C. T., 1975, ApJ, 202, 788

Dauser T., Wilms J., Reynolds C. S., Brenneman L. W., 2010, MNRAS, 409, 1534

Davis S. W., Hubeny I., 2006, ApJS, 164, 530

De Villiers J.-P., Hawley J. F., 2003, ApJ, 589, 458

Dexter J., 2011, PhD thesis, University of Washington

Dexter J., Agol E., 2009, ApJ, 696, 1616

Dexter J., Agol E., 2011, ApJ, 727, L24

Dexter J., Fragile P. C., 2011, ApJ, 730, 36

Dexter J., Quataert E., 2012, MNRAS, 426, L71

Dexter J., Agol E., Fragile P. C., 2009, ApJ, 703, L142

Dexter J., Agol E., Fragile P. C., McKinney J. C., 2010, ApJ, 717, 1092

Dexter J., Agol E., Fragile P. C., McKinney J. C., 2012a, J. Phys. Conf. Ser., 372, 012023

Dexter J., McKinney J. C., Agol E., 2012b, MNRAS, 421, 1517

Doeleman S. et al., 2009, in Astro2010: The Astronomy and Astrophysics Decadal Survey Vol, 2010, p. 68, preprint (arXiv:Astrophysics e-prints)

Doeleman S. S. et al., 2012, Science, 338, 355

Dolence J. C., Gammie C. F., Mościbrodzka M., Leung P. K., 2009, ApJS, 184, 387

Eisenhauer F. et al., 2008, in Proc. SPIE Conf. Ser. Vol. 7013, SPIE, Bellingham, p. 2

Falcke H., Goss W. M., Matsuo H., Teuben P., Zhao J., Zylka R., 1998, ApJ, 499, 731

Font J. A., Ibáñez J. M., Papadopoulos P., 1999, MNRAS, 305, 920

Gammie C. F., Leung P. K., 2012, ApJ, 752, 123

Gammie C. F., McKinney J. C., Tóth G., 2003, ApJ, 589, 444

Ginzburg V. L., Syrovatskii S. I., 1965, ARA&A, 3, 297

Ginzburg V. L., Syrovatskii S. I., 1969, ARA&A, 7, 375

Gold R., McKinney J. C., Johnson M. D., Doeleman S. S., 2016, preprint (arXiv:e-prints)

Hindmarsh A. C., 1983, in Stepleman R. S. et al., eds, Scientific Computing. p. 55

Huang L., Shcherbakov R. V., 2011, MNRAS, 416, 2574

Huang L., Liu S., Shen Z., Yuan Y., Cai M. J., Li H., Fryer C. L., 2009, ApJ, 703, 557

Johnson M. D. et al., 2015, Science, 350, 1242

Jones T. W., Hardee P. E., 1979, ApJ, 228, 268

Jones T. W., Odell S. L., 1977, ApJ, 214, 522

Krolik J. H., Hawley J. F., Hirose S., 2005, ApJ, 622, 1008

Kulkarni A. K. et al., 2011, MNRAS, 620

Landi Degl'Innocenti E., Landi Degl'Innocenti M., 1985, Sol. Phys., 97, 239

Legg M. P. C., Westfold K. C., 1968, ApJ, 154, 499

Li L.-X., Zimmerman E. R., Narayan R., McClintock J. E., 2005, ApJS, 157, 335

Luminet J.-P., 1979, A&A, 75, 228

Mahadevan R., Narayan R., Yi I., 1996, ApJ, 465, 327

Mao et al., 2016, in press

Melrose D. B., 1971, Ap&SS, 12, 172

Melrose D. B., 1980, Plasma Astrophysics. Nonthermal Processes in Diffuse Magnetized Plasmas – Vol.1: The Emission, Absorption and Transfer of Waves in Plasmas; Vol.2: Astrophysical Applications. Gordon and Breach, New York

Melrose D. B., 1997, J. Plasma Phys., 58, 735

Michel F. C., 1972, Ap&SS, 15, 153

Mościbrodzka M., Gammie C. F., Dolence J. C., Shiokawa H., Leung P. K., 2009, ApJ, 706, 497

Moscibrodzka M., Falcke H., Shiokawa H., 2015, preprint (arXiv:e-prints)

Noble S. C., Krolik J. H., 2009, ApJ, 703, 964

Noble S. C., Gammie C. F., McKinney J. C., Del Zanna L., 2006, ApJ, 641, 626

Noble S. C., Leung P. K., Gammie C. F., Book L. G., 2007, Class. Quantum Gravity, 24, 259

Noble S. C., Krolik J. H., Schnittman J. D., Hawley J. F., 2011, ApJ, 743, 115

Page D. N., Thorne K. S., 1974, ApJ, 191, 499

Pandya A., Zhang Z., Chandra M., Gammie C. F., 2016, preprint (arXiv:e-prints)

Rauch K. P., Blandford R. D., 1994, ApJ, 421, 46

Rees D. E., Durrant C. J., Murphy G. A., 1989, ApJ, 339, 1093

Rybicki G. B., Lightman A. P., 1979, Radiative Processes in Astrophysics, Wiley-Interscience, New York

Sazonov V. N., 1969, Sov. Astron., 13, 396

Schnittman J. D., Krolik J. H., 2009, ApJ, 701, 1175

Schnittman J. D., Krolik J. H., 2013, ApJ, 777, 11

Schnittman J. D., Krolik J. H., Hawley J. F., 2006, ApJ, 651, 1031

Shakura N. I., Sunyaev R. A., 1973, A&A, 24, 337

Shapiro S. L., 1973a, ApJ, 180, 531

Shapiro S. L., 1973b, ApJ, 185, 69

Shcherbakov R. V., 2008, ApJ, 688, 695

Shcherbakov R. V., Huang L., 2011, MNRAS, 410, 1052

Shcherbakov R. V., Penna R. F., McKinney J. C., 2012, ApJ, 755, 133

Sobolev V. V., 1963, A Treatise on Radiative Transfer

Viergutz S. U., 1993, A&A, 272, 355

Vincent F. H., Paumard T., Gourgoulhon E., Perrin G., 2011, Class. Quantum Gravity, 28, 225011

Walker M., Penrose R., 1970, Commun. Math. Phys., 18, 265

Westfold K. C., 1959, ApJ, 130, 241

Yuan F., Quataert E., Narayan R., 2003, ApJ, 598, 301

APPENDIX A: POLARISED SYNCHROTRON EMISSION AND ABSORPTION COEFFICIENTS FOR THERMAL AND POWER-LAW PARTICLE DISTRIBUTIONS

The subject of radiation from gyrating electrons in a magnetic field has been extensively studied, especially in the relativistic 'synchrotron' limit where the electron energy $\gamma \gtrsim 1$ (Westfold 1959; Ginzburg & Syrovatskii 1965, 1969; Legg & Westfold 1968; Sazonov 1969; Blumenthal & Gould 1970; Melrose 1971; Jones & Odell 1977; Rybicki & Lightman 1979). However, a consistent treatment of the derivation of the polarised emission and absorption coefficients for the two most commonly used particle distributions (thermal and power law) is still lacking.[2] This appendix gives examples of deriving the various coefficients from integrating the single particle polarised synchrotron emissivity over distributions of particles and provides approximate formulae for their evaluation. The results are compared to emissivities found in the literature and in some cases to numerical integration.

The Stokes basis in the emitting frame has $\mathbf{B} = (0, 0, 1)$, $\mathbf{e^1} = (-\cos\theta_B, 0, \sin\theta_B)$ and $\mathbf{e^2} = (0, 1, 0)$ where θ_B is the angle between B and the wave-vector $\boldsymbol{k}$ and $\mathbf{e^1}$, $\mathbf{e^2}$ are aligned with Stokes Q and U and the projection of B on to the Stokes basis is entirely along $\mathbf{e^2}$. Then the vacuum emissivity can be written as a rank-2 tensor (e.g. Melrose 1980):

$$\epsilon^{\alpha\beta} = \frac{\sqrt{3}e^2}{8\pi c} \nu_B \sin\theta_B H^{\alpha\beta}(\nu, \theta_B), \tag{A1}$$

where e is the electron charge, c is the speed of light, $\nu_B = \frac{eB}{2\pi mc}$, and

$$H^{11} = F\left(\frac{\nu}{\nu_c}\right) - G\left(\frac{\nu}{\nu_c}\right), \tag{A2}$$

$$H^{22} = F\left(\frac{\nu}{\nu_c}\right) + G\left(\frac{\nu}{\nu_c}\right), \tag{A3}$$

$$H^{12} = -H^{21} = \frac{4\mathrm{i}\cot\theta_B}{3\gamma} H\left(\frac{\nu}{\nu_c}\right), \tag{A4}$$

where ν is the emitted frequency, γ is the electron Lorentz factor, $\nu_c = 3/2\nu_B\sin\theta_B\gamma^2$ and

$$F(x) = x\int_x^\infty \mathrm{d}y K_{5/3}(y), \tag{A5}$$

$$G(x) = x K_{2/3}(x), \tag{A6}$$

$$H(x) = \int_x^\infty \mathrm{d}y K_{1/3}(y) + x K_{1/3}(x), \tag{A7}$$

are the synchrotron functions for total, linearly and circularly polarised emission respectively and $K_\alpha(z)$ is the modified Bessel function.

To compute the emissivity from a distribution of electrons, these formulae are integrated over the particle distribution:

$$j^{\alpha\beta} = \int_0^\infty \mathrm{d}\gamma N(\gamma)\epsilon^{\alpha\beta}. \tag{A8}$$

The Stokes emissivities are then given as $j_I = j^{22} + j^{11}$, $j_Q = j^{22} - j^{11}$, $j_U = j_{12} + j_{12}$, and $j_V = i(j_{12} - j_{21})$. For this Stokes basis, j_U vanishes.

The two most commonly used particle distributions for astrophysical sources are the relativistic thermal (Maxwell) distribution,

$$N(\gamma) = \frac{n\gamma^2\beta \exp(-\gamma/\theta_e)}{\theta_e K_2(1/\theta_e)}, \tag{A9}$$

where n is the electron number density and $\theta_e = \frac{kT}{mc^2}$ is the dimensionless electron temperature; and the power-law distribution,

$$N(\gamma) = \begin{cases} n(p-1)(\gamma_1^{1-p} - \gamma_2^{1-p})^{-1}\gamma^{-p} & \gamma_1 < \gamma < \gamma_2 \\ 0 & \text{otherwise} \end{cases},$$

where $\gamma_{1,2}$ are the low- and high-energy cutoffs of the distribution.

We consider these two cases in turn and derive approximate formulae for their evaluation.

A1 Ultrarelativistic thermal distribution

For the thermal distribution, substituting equation (A9) into equation (A8) with $\beta \simeq 1$ and $\theta_e \gg 1$ gives,

$$j^{\alpha\beta} = \frac{\sqrt{3}ne^2\nu_B \sin\theta_B}{8\pi\theta_e(2\theta_e^2)} \int_0^\infty \mathrm{d}\gamma \gamma^2 \exp(-\gamma/\theta_e)H^{\alpha\beta}(\nu, \theta_B), \tag{A10}$$

[2] This issue is also addressed in detail by Pandya et al. (2016).

where the approximate form of the modified Bessel function for small argument $K_2(z) \to 2z^2$ was used. First substitute $z \equiv \gamma/\theta_e$ so that,

$$j^{\alpha\beta} = \frac{\sqrt{3}ne^2\nu_B \sin\theta_B \theta_e^2}{8\pi c(2\theta_e^2)} \int_0^\infty dz z^2 \exp(-z) H^{\alpha\beta}(\nu, \theta_B). \tag{A11}$$

Then substitute γ for z in the synchrotron functions and use the relations between $j^{\alpha\beta}$ and $j_{I,Q,V}$ to find:

$$j_I(\nu, \theta_B) = \frac{ne^2\nu}{2\sqrt{3}c\theta_e^2} I_I(x), \tag{A12}$$

$$j_Q(\nu, \theta_B) = \frac{ne^2\nu}{2\sqrt{3}c\theta_e^2} I_Q(x), \tag{A13}$$

$$j_V(\nu, \theta_B) = \frac{2ne^2\nu \cot\theta_B}{3\sqrt{3}c\theta_e^3} I_V(x), \tag{A14}$$

where $x \equiv \nu/\nu_c$ and here θ_e takes the place of γ in the definition of ν_c, and the thermal synchrotron integrals are,

$$I_I(x) = \frac{1}{x} \int_0^\infty dz z^2 \exp(-z) F\left(\frac{x}{z^2}\right), \tag{A15}$$

$$I_Q(x) = \frac{1}{x} \int_0^\infty dz z^2 \exp(-z) G\left(\frac{x}{z^2}\right), \tag{A16}$$

$$I_V(x) = \frac{1}{x} \int_0^\infty dz z \exp(-z) H\left(\frac{x}{z^2}\right). \tag{A17}$$

where the function $I_I(x)$ corresponds to $I(x_M)$ from Mahadevan et al. (1996). This result agrees with the formulae from previous work (Sazonov 1969; Mahadevan et al. 1996; Huang et al. 2009). The integrals can be approximated analytically with high accuracy by matching the asymptotic behaviour for small and large arguments and fitting polynomials in the transition region (Mahadevan et al. 1996). We find the following approximate forms,

$$I_I(x) = 2.5651(1 + 1.92x^{-1/3} + 0.9977x^{-2/3}) \exp(-1.8899x^{1/3}), \tag{A18}$$

$$I_Q(x) = 2.5651(1 + 0.932x^{-1/3} + 0.4998x^{-2/3}) \exp(-1.8899x^{1/3}), \tag{A19}$$

$$I_V(x) = (1.8138x^{-1} + 3.423x^{-2/3} + 0.02955x^{-1/2} + 2.0377x^{-1/3}) \exp(-1.8899x^{1/3}), \tag{A20}$$

all agree with numerical integration within $\lesssim 1$ per cent for all x. We further compare the results to numerical integration of the full emissivities using the public SYMPHONY[3] code (Pandya et al. 2016). All fitting functions are accurate to within $\lesssim 20$ per cent for parameters of interest ($\theta_e > 3$, $\nu/\nu_c > 1$), but our circular polarisation emissivity has larger deviations at low temperature ($\theta_e < 1$).

The absorption coefficients are computed from the emission coefficients assuming local thermodynamic equilibrium so that Kirchoff's Law, $j_\nu = \alpha_\nu B_\nu$, holds with B_ν the blackbody function (e.g. Rybicki & Lightman 1979).

A2 Power-law distribution

In this case, after plugging in the distribution we change the variable of integration to $x \equiv \nu/\nu_c$:

$$j^{\alpha\beta} = \frac{(p-1)ne^2\nu_p}{4\sqrt{3}c\left(\gamma_1^{1-p} - \gamma_2^{1-p}\right)} \left(\frac{\nu}{\nu_p}\right)^{-\frac{p-1}{2}} \int_{x_1}^{x_2} dx\, x^{\frac{p-3}{2}} H^{\alpha\beta}(\nu, \theta_B), \tag{A21}$$

where $\nu_p = \nu_c/\gamma^2$. Then the three emissivities can be written:

$$j_I = \frac{ne^2(p-1)\nu_p}{2\sqrt{3}c\left(\gamma_1^{1-p} - \gamma_2^{1-p}\right)} \left(\frac{\nu}{\nu_p}\right)^{-\frac{p-1}{2}} [G_I(x_1) - G_I(x_2)], \tag{A22}$$

$$j_Q = \frac{ne^2(p-1)\nu_p}{2\sqrt{3}c\left(\gamma_1^{1-p} - \gamma_2^{1-p}\right)} \left(\frac{\nu}{\nu_p}\right)^{-\frac{p-1}{2}} [G_Q(x_1) - G_Q(x_2)], \tag{A23}$$

---

[3] https://github.com/afd-illinois/symphony

$$j_V = \frac{2ne^2(p-1)\nu_p \cot\theta_B}{3\sqrt{3}c\left(\gamma_1^{1-p} - \gamma_2^{1-p}\right)} \left(\frac{\nu}{\nu_p}\right)^{-\frac{p}{2}} [G_V(x_1) - G_V(x_2)],$$ (A24)

where the power-law synchrotron integrals are,

$$G_I(x) = \int_x^\infty dz z^{\frac{p-3}{2}} F(z),$$ (A25)

$$G_Q(x) = \int_x^\infty dz z^{\frac{p-3}{2}} G(z),$$ (A26)

$$G_V(x) = \int_x^\infty dz z^{\frac{p}{2}-1} H(z).$$ (A27)

In many prior studies (Legg & Westfold 1968; Blumenthal & Gould 1970; Melrose 1971; Jones & Odell 1977) the integrals are performed analytically for the frequency range $\gamma_1^2 \nu_p \ll \nu \ll \gamma_2^2 \nu_p$ where the limits of integration, $x_{1,2} = \nu/(\gamma_{1,2}^2 \nu_p)$ can be extended to 0 and ∞.

For the primary non-thermal source of interest, M87,

$$\gamma_1^2 \nu_p \sim 2 \times 10^{11} \left(\frac{B}{10\,G}\right) \left(\frac{\gamma_1}{100}\right)^2 \text{Hz},$$ (A28)

uncomfortably close to frequencies $\simeq 230$ GHz of interest for mm-VLBI (Doeleman et al. 2012; Akiyama et al. 2015) for $\gamma_1 \gtrsim 30$. We then keep the finite limits of integration and numerically tabulate the integrals G_I, G_Q and G_V as functions of x for select values of $p = 3.0, 3.5, 7.0$ currently. This procedure can be sped up significantly using the relation (Westfold 1959),

$$L(x; s, \alpha) \equiv \int_x^\infty d\xi \xi^{s-1} \int_\xi^\infty dy K_{\alpha+1}(y)$$

$$= \frac{\alpha+s}{s} \int_x^\infty d\xi \xi^{s-1} K_\alpha(\xi) - \frac{x^s}{s} \left[\int_x^\infty dy K_{\alpha+1}(y) - K_\alpha(x)\right]$$ (A29)

to reduce the double integrals to single integrals. The results agree with those in Legg & Westfold equation (33) after using a recurrence relation,

$$2K'_\alpha(x) = -(K_{\alpha+1} + K_{\alpha-1}),$$ (A30)

and noting that $K_{-\alpha}(x) = K_\alpha(x)$ to transform the Bessel functions in $H(x)$.

To check against approximate formulae elsewhere, we extend the limits of integration to 0 and ∞ and use,

$$I(s, \alpha) \equiv \int_0^\infty dx x^s K_\alpha(x) = 2^{s-1} \Gamma\left(\frac{s+\alpha+1}{2}\right) \Gamma\left(\frac{s-\alpha+1}{2}\right)$$ (A31)

$$J(s, \alpha) \equiv L(0; s+1, \alpha-1) = \frac{\alpha+s}{s+1} I(s, \alpha-1)$$

$$= \frac{\alpha+s}{s+1} 2^{s-1} \Gamma\left(\frac{s+\alpha}{2}\right) \Gamma\left(\frac{s-\alpha}{2}+1\right)$$ (A32)

to find the approximate forms $G_{I,Q,V}(0) - G_{I,Q,V}(\infty)$:

$$G_I(0) = J\left(\frac{p-1}{2}, \frac{5}{3}\right) = \frac{2^{\frac{p-3}{2}}(p+7/3)}{p+1} \Gamma\left(\frac{p}{4} + \frac{7}{12}\right) \Gamma\left(\frac{p}{4} - \frac{1}{12}\right),$$ (A33)

$$G_Q(0) = I\left(\frac{p-1}{2}, \frac{2}{3}\right) = \frac{p+1}{p+7/3} G_I(0),$$ (A34)

$$G_V(0) = J\left(\frac{p}{2} - 1, \frac{1}{3}\right) + I\left(\frac{p}{2}, \frac{1}{3}\right)$$

$$= \frac{2^{\frac{p}{2}-1}(p+2)}{p} \Gamma\left(\frac{p}{4} + \frac{1}{3}\right) \Gamma\left(\frac{p}{4} + \frac{2}{3}\right),$$ (A35)

$$G_{I,Q,V}(\infty) = 0$$ (A36)

leading to the approximate emissivities:

$$j_I^0 = \frac{ne^2(p-1)\nu_p}{2\sqrt{3}c\left(\gamma_1^{1-p} - \gamma_2^{1-p}\right)} \left(\frac{\nu}{\nu_p}\right)^{-\frac{p-1}{2}} 2^{\frac{p-3}{2}} \frac{p+7/3}{p+1} \Gamma\left(\frac{p}{4} + \frac{7}{12}\right) \Gamma\left(\frac{p}{4} - \frac{1}{12}\right),$$ (A37)

$$j_Q^0 = \frac{p+1}{p+7/3} j_I^0,$$ (A38)

$$j_V^0 = \frac{2ne^2(p-1)\nu_p \cot\theta_B}{3\sqrt{3}c\left(\gamma_1^{1-p} - \gamma_2^{1-p}\right)} \left(\frac{\nu}{\nu_p}\right)^{-\frac{p}{2}} 2^{\frac{p}{2}-1} \frac{p+2}{p} \Gamma\left(\frac{p}{4} + \frac{1}{3}\right) \Gamma\left(\frac{p}{4} + \frac{2}{3}\right).$$ (A39)

These results agree with those of several authors.

In the case of non-thermal emission, the absorption coefficient cannot be simply related to the emissivity using Kirchoff's Law, and instead we use (Melrose 1980):

$$\alpha^{\alpha\beta} = -\frac{c}{m\nu^2} \int_0^\infty d\gamma\, \gamma^2 \frac{d}{d\gamma}\left[\frac{N(\gamma)}{\gamma^2}\right] \eta^{\alpha\beta}(\gamma, \nu, \theta_B).$$ (A40)

The derivation is analogous to that for the emissivity, and the results are:

$$\alpha_I = \frac{ne^2(p-1)(p+2)}{4\sqrt{3}mc\nu_p\left(\gamma_1^{1-p} - \gamma_2^{1-p}\right)} \left(\frac{\nu}{\nu_p}\right)^{-\frac{p}{2}-2} [Ga_I(x_1) - Ga_I(x_2)],$$ (A41)

$$\alpha_Q = \alpha_I \frac{[Ga_Q(x_1) - Ga_Q(x_2)]}{[Ga_I(x_1) - Ga_I(x_2)]},$$ (A42)

$$\alpha_V = \frac{ne^2(p-1)(p+2)\cot\theta_B}{3\sqrt{3}mc\nu_p\left(\gamma_1^{1-p} - \gamma_2^{1-p}\right)} \left(\frac{\nu}{\nu_p}\right)^{-\frac{p+5}{2}} [Ga_V(x_1) - Ga_V(x_2)],$$ (A43)

where the power-law absorption integrals are,

$$Ga_I(x) = \int_x^\infty dz\, z^{\frac{p}{2}-1} F(z),$$ (A44)

$$Ga_Q(x) = \int_x^\infty dz\, z^{\frac{p}{2}-1} G(z),$$ (A45)

$$Ga_V(x) = \int_x^\infty dz\, z^{\frac{p-1}{2}} H(z).$$ (A46)

Again extending the limits of integration, we find agreement with approximate formulae in the literature:

$$Ga_I(0) = \frac{p+10/3}{p+2} 2^{\frac{p}{2}-1} \Gamma\left(\frac{p}{4} + \frac{5}{6}\right) \Gamma\left(\frac{p}{4} + \frac{1}{6}\right),$$ (A47)

$$Ga_Q(0) = \frac{p+2}{p+10/3} Ga_I(0)$$ (A48)

$$Ga_V(0) = \frac{p+3}{p+1} 2^{\frac{p-1}{2}} \Gamma\left(\frac{p}{4} + \frac{7}{12}\right) \Gamma\left(\frac{p}{4} + \frac{11}{12}\right),$$ (A49)

$$Ga_{I,Q,V}(\infty) = 0.$$ (A50)

Combining the approximate forms of the emission and absorption coefficients shows that the power-law synchrotron source function $S_\nu \sim \nu^{5/2}$ (e.g. Rybicki & Lightman 1979), compared to $S_\nu = B_\nu \sim \nu^2$ in the thermal case. Fig. A1 compares numerical integration of the formulae in equations (A22) and (A42) with the forms from the literature. At low frequencies $\nu \lesssim \gamma_1^2 \nu_p$, the source function drops more steeply than expected from $\sim \nu^{5/2}$.
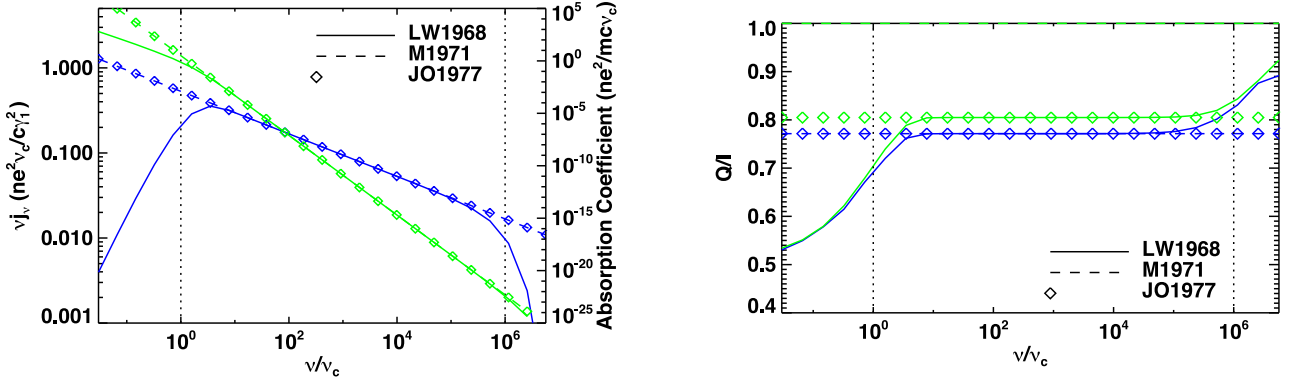
Figure A1. Left: total emission (blue) and absorption (green) coefficients from this work and Legg & Westfold (solid), Melrose (dashed) and Jones & Odell (diamonds). Right: linear polarisation fraction in emission (blue) and absorption (green) coefficients from this work and Legg & Westfold (solid), Melrose (dashed) and Jones & Odell (diamonds). Here, $\nu_c \equiv \nu_p \gamma_1^2$ and the dotted lines show the locations of $\nu/\nu_c = 1$, γ_2^2/γ_1^2, where the approximate forms of the coefficients lose accuracy.

APPENDIX B: FARADAY COEFFICIENTS FOR POWER-LAW AND THERMAL DISTRIBUTIONS OF ELECTRONS

As well as the emission and absorption coefficients calculated above (Appendix A), the coefficients ρ_V and ρ_Q affect the generation and transfer of polarisation in a magnetized plasma. We use approximate expressions from the literature for these coefficients which as above are modified to (i) be fast to evaluate and (ii) have the correct asymptotic limits.

B1 Power-law distribution

In the case of a power-law distribution, we use the expressions from Jones & Odell ([1977](#)) Appendix C, written in our notation:

$$\rho_Q = -\rho_\perp \left(\frac{\nu_B \sin \theta_B}{\nu} \right)^3 \gamma_1^{2-p} \left[\left(1 - \left(\frac{2\nu_1}{3\nu} \right)^{p/2-1} \right) (p/2 - 1)^{-1} \right], \tag{B1}$$

$$\rho_V = 2 \frac{p+2}{p+1} \rho_\perp \left(\frac{\nu_B \sin \theta_B}{\nu} \right)^2 \gamma_1^{-(p+1)} \ln \gamma_1 \cot \theta_B, \tag{B2}$$

$$\rho_\perp = \frac{ne^2}{mc\nu_B \sin \theta_B} (p-1) \left[\gamma_1^{1-p} - \gamma_2^{1-p} \right]^{-1}. \tag{B3}$$

More accurate expressions (Huang & Shcherbakov [2011](#)) require integration over the distribution function and for this reason are slow to evaluate. These approximate forms are relatively accurate for $\gamma_1 \lesssim 10^2$ (left-hand panel of fig. 6 in Huang & Shcherbakov [2011](#)). In the example semi-analytic jet problem above, Faraday rotation and conversion are negligible (Broderick & Loeb [2009](#)). None the less, it should be possible to find accurate fitting functions for these coefficients, which would be consistent with our approach for the other coefficients.

B2 Thermal distribution

Faraday coefficients for thermal distributions of electrons have been calculated in limits of either high frequency $\nu/\nu_c \gg 1$ (e.g. Melrose [1997](#)), at high temperatures $\theta_e \gg 1$, or both. In particular, Shcherbakov ([2008](#)) provided approximate fitting functions for ρ_V and ρ_Q over a wide temperature range $\theta_e \gtrsim 1$ with high accuracy for $\nu/\nu_c \gtrsim 10^{-1}$ (their equations 25, 26, 33, but in our notation):

$$\rho_Q = \frac{ne^2 \nu_B^2 \sin \theta_B^2}{mc\nu^3} f(X) \left[\frac{K_1(\theta_e^{-1})}{K_2(\theta_e^{-1})} + 6\theta_e \right] \tag{B4}$$

$$\rho_V = \frac{2ne^2 \nu_B}{mc\nu^2} \frac{K_0(\theta_e^{-1})}{K_2(\theta_e^{-1})} \cos \theta_B \, g(X), \tag{B5}$$

where

$$f(X) = 2.011 \exp\left(-\frac{X^{1.035}}{4.7} \right) - \cos\left(\frac{X}{2} \right) \exp\left(-\frac{X^{1.2}}{2.73} \right) - 0.011 \exp\left(-\frac{X}{47.2} \right) \tag{B6}$$

$$g(X) = 1 - 0.11 \ln(1 + 0.035X) \tag{B7}$$

$$X = \left(\frac{3}{2\sqrt{2}} 10^{-3} \frac{\nu}{\nu_c} \right)^{-1/2}, \tag{B8}$$
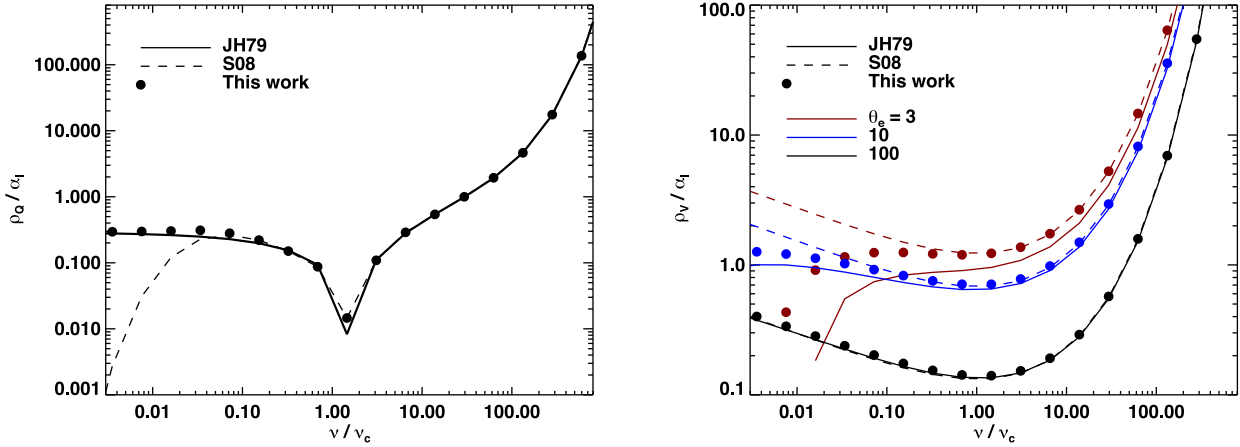
Figure B1. Left: ratio of thermal Faraday conversion coefficient to total absorption as a function of ν/ν_c with $\theta_e = 100$ and $\theta_B = \pi/4$ calculated from numerical integration of the expression in Jones & Hardee (1979) [solid line, equation (B9)], the fitting function approach introduced by Shcherbakov (2008) [dashed line, equation (B4)], and in this work [black dots, equation (B13)]. Right: same as the left-hand panel but for Faraday rotation at three different temperatures. In both cases all results agree at high frequencies and temperatures. Our fitting functions use the temperature dependence from Shcherbakov (2008) and the low-frequency limits from Jones & Hardee (1979).

and their parameter X is a function of ν/ν_c. In the high-frequency limit $\nu/\nu_c \gg 1$, both functions asymptotically reach unity. The cosine term in $f(X)$ is used to fit the sign change in ρ_Q near $\nu/\nu_c \simeq 1.5$.

While the high frequency and high temperature limit is most relevant for our applications of interest, e.g. modelling the submm emission from Sgr A*, ideally we would have expressions that are correct in both asymptotic limits. For this reason we modify the expressions in Shcherbakov (2008), by comparing them with the expressions for the high temperature synchrotron limit given in Jones & Hardee (1979) [their equations (3)– (4), in our notation]:

$$\rho_Q = \frac{\pi n e^2 (\nu/\nu_c)^{-2/3}}{2^{4/3} 3^{2/3} m c \theta_e^3 \nu} J_4(\nu/\nu_c),$$

(B9)

$$\rho_V = \frac{n e^2 \nu_B \cos\theta_B}{m c \nu^2 \theta_e^2} J_5(\nu/\nu_c, \theta_e, \theta_B),$$

(B10)

where

$$J_4(z) = \int_0^\infty dy\, y^{4/3} Gi'(q) e^{-y},$$

(B11)

$$J_5(z, \theta_e, \theta_B) = \int_0^\infty dy \left[\ln(y\theta_e) + \sin\theta_B \ln 2 + 1/3 [q\pi Gi(q) - 1] + 1/2 \int_q^\infty dx\, (\pi Gi(x) - 1/x) \right] e^{-y},$$

(B12)

and where $q \equiv (3/2z/y^2)^{2/3}$ and $Gi(x)$ is defined in terms of Airy functions (Abramowitz & Stegun 1970).

In the high-frequency, high temperature limit where $\nu/\nu_c \gg 1$, $\theta_e \gg 1$, and where we can replace the Bessel functions by their asymptotic limits and $J_4 \to -24/\pi (3/2z)^{-4/3}$, $J_5 \to \ln\theta_e$, these expressions agree with the above results from Shcherbakov (2008). From numerically integrating $J_4(z)$ and $J_5(z)$, we also find good agreement between the two sets of coefficients over their reported ranges of validity. We adapt the fitting function $f(X)$ in Shcherbakov (2008) to use the asymptotic limit of ρ_Q at small ν/ν_c, where $J_4(z) \to \frac{4}{9 \times 3^{5/6}}$:

$$f_m(X) = f(X) + \left[0.011 \exp\left(-\frac{X}{47.2}\right) - 2^{-1/3}/3^{23/6} 10^4 \pi X^{-8/3} \right] 1/2 \left[1 + \tanh(10 \ln x/120) \right].$$

(B13)

The added term imposes the correct asymptotic limit at large X (small ν/ν_c) and for this reason maintains good accuracy over all ν/ν_c where the synchrotron limit is valid ($\nu/\nu_B \gg 1$).

For ρ_V, the term $J5(\nu/\nu_c)$ from Jones & Hardee (1979) separates into a sum of terms which depend on temperature and θ_B, and those which only depend on ν/ν_c. This suggests that it would be better to use the factor $g(X)$ in Shcherbakov (2008) as a difference from the high-frequency limit rather than a multiplication:

$$\rho_V = \frac{2 n e^2 \nu_B \cos\theta_B}{m c \nu^2} \frac{K_0(\theta_e^{-1}) - \Delta J_5(X)}{K_2(\theta_e^{-1})},$$

(B14)

where we define our correction factor $\Delta J_5(X)$ in a similar spirit to that of Shcherbakov (2008), but modified for higher accuracy:

$$\Delta J_5(X) = 0.4379 \ln(1 + 0.001\,858 X^{1.503}).$$

(B15)

Fig. B1 compares numerical integration of equation (B9) (Jones & Hardee 1979) with the fitting functions from equation (B4) (Shcherbakov 2008) and our modified forms. Our approximate versions are fast to compute, while maintaining accuracy over all ν/ν_c for $\nu/\nu_B \gg 1$.

We have compared polarised spectra and maps from HARM models of Sgr A* computed using the prescriptions from Shcherbakov ([2008](#)), Jones & Hardee ([1979](#)), and the high temperature, high frequency limit. As expected, all expressions are in excellent agreement when $\nu/\nu_c \gg 1$, in this case for $\nu \gtrsim 10^{12}$ Hz. Below that, our modified expressions and those from Shcherbakov ([2008](#)) are in good agreement, while the degree of circular polarisation can differ between our results and the high-frequency limit. As described in the main text, models of Sgr A* in the submm have self-absorption optical depth $\tau_I \gtrsim 1$, $\nu/\nu_c \sim 10 - 100$, and $\theta_e \sim 10$, so that the Faraday optical depths can be very large and have an important effect on the resulting polarisation maps and spectra (e.g. Fig. [8](#)). Since this result is for the high-frequency, relativistic limit, it does not depend on the fitting function used.

APPENDIX C: ANALYTIC SOLUTIONS TO THE POLARISED RADIATIVE TRANSFER EQUATIONS

This appendix provides the analytic solutions to the polarised radiative transfer equations used for testing different integration methods for GRTRANS in Section 3.2. In all cases, the boundary condition used is that the initial intensity is zero for each Stokes parameter.

The first case considered is pure emission and absorption in stokes I and Q, in which case equation (47) becomes:

$$\frac{\mathrm{d}}{\mathrm{d}s}\begin{pmatrix} I \\ Q \end{pmatrix} = \begin{pmatrix} j_I \\ j_Q \end{pmatrix} - \begin{pmatrix} \alpha_I & \alpha_Q \\ \alpha_Q & \alpha_I \end{pmatrix} \begin{pmatrix} I \\ Q \end{pmatrix}, \tag{C1}$$

whose solution is,

$$I(s) = \frac{1}{\alpha(\alpha_I - \alpha_Q)} \left\{ (j_I\alpha_I - j_Q\alpha_Q) \left[1 - \frac{\mathrm{e}^{-\alpha s}}{2}(1 + \mathrm{e}^{2\alpha_Q s}) \right] + (j_I\alpha_Q - j_Q\alpha_I)\frac{\mathrm{e}^{-\alpha s}}{2}(1 - \mathrm{e}^{2\alpha_Q s}) \right\}, \tag{C2}$$

$$Q(s) = \frac{1}{\alpha(\alpha_I - \alpha_Q)} \left\{ (j_Q\alpha_I - j_I\alpha_Q) \left[1 - \frac{\mathrm{e}^{-\alpha s}}{2}\left(1 + \mathrm{e}^{2\alpha_Q s}\right) \right] + (j_Q\alpha_Q - j_I\alpha_I)\frac{\mathrm{e}^{-\alpha s}}{2}\left(1 - \mathrm{e}^{2\alpha_Q s}\right) \right\}, \tag{C3}$$

where $\alpha \equiv \alpha_I + \alpha_Q$. When $\alpha_Q = 0$, the second group of terms in each equation vanishes while the first reduces to the usual formal solution of the radiative transfer equation, e.g. when stokes I and Q are not coupled. Examples of the solution are shown in Fig. [3](#).

The second case of interest is pure polarised emission in Stokes (Q, U, V) along with Faraday rotation and conversion ($\rho_{Q,V}$). Here the polarised radiative transfer equation is,

$$\frac{\mathrm{d}}{\mathrm{d}s}\begin{pmatrix} Q \\ U \\ V \end{pmatrix} = \begin{pmatrix} j_Q \\ j_U \\ j_V \end{pmatrix} - \begin{pmatrix} 0 & \rho_V & 0 \\ -\rho_V & 0 & \rho_Q \\ 0 & -\rho_Q & 0 \end{pmatrix} \begin{pmatrix} Q \\ U \\ V \end{pmatrix}, \tag{C4}$$

where we have set $\rho_U = 0$ as is commonly chosen for the Stokes basis for synchrotron radiation. From this equation it is apparent that ρ_V is responsible for changing the linear polarisation direction (mixing stokes Q and U, Faraday rotation) while ρ_Q converts between linear and circular polarisation (mixing stokes U and V, Faraday conversion). The solution is,

$$Q(s) = \frac{\rho_Q}{\rho^2}(j_Q\rho_Q + j_V\rho_V)s - \frac{\rho_V}{\rho^3}(j_V\rho_Q - j_Q\rho_V)\sin\rho s - \frac{j_U\rho_V}{\rho^2}(1 - \cos\rho s), \tag{C5}$$

$$U(s) = \frac{j_Q\rho_V - j_V\rho_Q}{\rho^2}(1 - \cos\rho s) + \frac{j_U}{\rho}\sin\rho s, \tag{C6}$$

$$V(s) = \frac{\rho_V}{\rho^2}(j_Q\rho_Q + j_V\rho_V)s - \frac{\rho_Q}{\rho^3}(j_Q\rho_V - j_V\rho_Q)\sin\rho s + \frac{j_U\rho_Q}{\rho^2}(1 - \cos\rho s), \tag{C7}$$

where $\rho \equiv \sqrt{\rho_Q^2 + \rho_V^2}$. These solutions for a sample case are plotted in Fig. [4](#).

In the case of only Faraday rotation or conversion ($\rho_Q = 0$ for Stokes Q or $\rho_V = 0$ for Stokes V), the solution is purely oscillatory with the maximum linearly polarised intensity restricted to be $\sim j/\rho$ independent of the total intensity or path length, despite the fact that there is no absorption. Since in this optically thin limit the total intensity grows as $j_I s$, the fractional polarisation decreases as $1/s$. When both Faraday rotation and conversion are present, the Stokes Q and V acquire terms which linearly increase with s, while the oscillatory terms still have maximum values that are independent of s. This means that in the limit of large Faraday optical depth (large s), the fractional polarisation approaches a constant value $Q, V/I = \rho_{Q,V}(j_Q\rho_Q + j_V\rho_V)/j_I\rho^2$ instead of decreasing as $1/s$ in the pure Faraday rotation or conversion case. Since for cases of interest $\rho_V > \rho_Q$, circular polarisation becomes dominant over linear polarisation in the limit of large Faraday optical depth.

This is a different limit than an initial polarised intensity travel through a magnetised medium where Faraday rotation occurs. In that case, the intensity also oscillates between Stokes Q and U, but with a constant polarised intensity. The fractional polarisation only decreases when the Faraday rotation is instead occurring in the region where the polarised emission is being produced.

APPENDIX D: CLOSED FORM EXPRESSION FOR O(s, s')

Landi Degl'Innocenti & Landi Degl'Innocenti ([1985](#)) found a closed form solution for the matrix operator **O**(s, s'), defined by

$$\frac{\mathrm{d}}{\mathrm{d}s}\mathbf{O}(s, s') = -\mathbf{K}(s)\mathbf{O}(s, s'), \qquad \mathbf{O}(s, s) = 1, \tag{D1}$$

which describes the transfer of the Stokes parameters from position s to s' in the absence of emission, which is valid under limited conditions including when the absorption matrix **K** is constant over the interval. We reproduce the solution here in our notation:

$$\mathbf{O}(s, s') = \exp(-\alpha_I \Delta s) \left\{ [\cosh(\Lambda_1 \Delta s) + \cos(\Lambda_2 \Delta s)] \mathbf{M}_1/2 - \sin(\Lambda_2 \Delta s)\mathbf{M}_2 - \sinh(\Lambda_1 \Delta s)\mathbf{M}_3 + [\cosh(\Lambda_1 \Delta s) - \cos(\Lambda_2 \Delta s)] \mathbf{M}_4/2 \right\},$$

(D2)

where

$$\mathbf{M}_1 = \mathbf{1}$$

(D3)

$$\mathbf{M}_2 = \frac{1}{\Theta}\begin{pmatrix} 0 & \Lambda_2\alpha_Q - \sigma\Lambda_1\rho_Q & \Lambda_2\alpha_U - \sigma\Lambda_1\rho_U & \Lambda_2\alpha_V - \sigma\Lambda_1\rho_V \\ \Lambda_2\alpha_Q - \sigma\Lambda_1\rho_Q & 0 & \sigma\Lambda_1\alpha_V + \Lambda_2\rho_V & -\sigma\Lambda_1\alpha_U - \Lambda_2\rho_U \\ \Lambda_2\alpha_U - \sigma\Lambda_1\rho_U & -\sigma\Lambda_1\alpha_V - \Lambda_2\rho_V & 0 & \sigma\Lambda_1\alpha_Q + \Lambda_2\rho_Q \\ \Lambda_2\alpha_V - \sigma\Lambda_1\rho_V & \sigma\Lambda_1\alpha_U + \Lambda_2\rho_U & -\sigma\Lambda_1\alpha_Q - \Lambda_2\rho_Q & 0 \end{pmatrix}$$

(D4)

$$\mathbf{M}_3 = \frac{1}{\Theta}\begin{pmatrix} 0 & \Lambda_1\alpha_Q + \sigma\Lambda_2\rho_Q & \Lambda_1\alpha_U + \sigma\Lambda_2\rho_Q & \Lambda_1\alpha_V + \sigma\Lambda_2\rho_V \\ \Lambda_1\alpha_Q + \sigma\Lambda_2\rho_Q & 0 & -\sigma\Lambda_2\alpha_V + \Lambda_1\rho_V & \sigma\Lambda_2\alpha_U - \Lambda_1\rho_U \\ \Lambda_1\alpha_U + \sigma\Lambda_2\rho_U & \sigma\Lambda_2\alpha_V - \Lambda_1\rho_V & 0 & -\sigma\Lambda_2\alpha_Q + \Lambda_1\rho_Q \\ \Lambda_1\alpha_V + \sigma\Lambda_2\rho_V & -\sigma\Lambda_2\alpha_U + \Lambda_1\rho_U & \sigma\Lambda_2\alpha_Q - \Lambda_1\rho_Q & 0 \end{pmatrix}$$

(D5)

$$\mathbf{M}_4 = \frac{2}{\Theta}\begin{pmatrix} (\alpha^2 + \rho^2)/2 & \alpha_V\rho_U - \alpha_U\rho_V & \alpha_Q\rho_V - \alpha_V\rho_Q & \alpha_U\rho_Q - \alpha_Q\rho_U \\ \alpha_U\rho_V - \alpha_V\rho_U & \alpha_Q^2 + \rho_Q^2 - (\alpha^2 + \rho^2)/2 & \alpha_Q\alpha_U + \rho_Q\rho_U & \alpha_V\alpha_Q + \rho_V\rho_Q \\ \alpha_V\rho_Q - \alpha_Q\rho_V & \alpha_Q\alpha_U + \rho_Q\rho_U & \alpha_U^2 + \rho_U^2 - (\alpha^2 + \rho^2)/2 & \alpha_U\alpha_V + \rho_U\rho_V \\ \alpha_Q\rho_U - \alpha_U\rho_Q & \alpha_V\alpha_Q + \rho_V\rho_Q & \alpha_U\alpha_V + \rho_U\rho_V & \alpha_V^2 + \rho_V^2 - (\alpha^2 + \rho^2)/2 \end{pmatrix}$$

(D6)

and

$$\Theta = 2 \left[(\alpha^2 - \rho^2)^2/4 + (\alpha \cdot \rho)^2 \right]^{1/2},$$

(D7)

$$\Lambda_{1,2} = \left\{ \left[(\alpha^2 - \rho^2)^2/4 + (\alpha \cdot \rho)^2 \right]^{1/2} \pm (\alpha^2 - \rho^2)/2 \right\}^{1/2},$$

(D8)

$$\sigma = \text{sign}(\alpha \cdot \rho),$$

(D9)

$$\alpha \cdot \rho = \alpha_Q\rho_Q + \alpha_U\rho_U + \alpha_V\rho_V,$$

(D10)

$$\rho^2 = \rho_Q^2 + \rho_U^2 + \rho_V^2,$$

(D11)

$$\alpha^2 = \alpha_Q^2 + \alpha_U^2 + \alpha_V^2.$$

(D12)

This paper has been typeset from a TeX/LaTeX file prepared by the author.